X-ray Scattering Study of the Critical Behavior of the Second Harmonic in the Density Wave System 7APCBB

by

Yongmei Shao

Submitted to the Department of Physics
in partial fulfillment of the requirements for the degree of

Master of Science

at the

MASSACHUSETTS INSTITUTE OF TECHNOLOGY

August 1994

Author ....
Department of Physics
August 5th, 1994

Certified by ....
Robert J. Birgeneau
Cecil and Ida Green Professor of Physics Dean of Science
Thesis Supervisor

Accepted by ....
George F. Koster
Chairman, Departmental Committee on Graduate Students

X-ray Scattering Study of the Critical Behavior of the Second Harmonic in the Density Wave System 7APCBB

by

Yongmei Shao

Submitted to the Department of Physics
on August 5th, 1994, in partial fulfillment of the
requirements for the degree of
Master of Science

Abstract

In this thesis, we report a high resolution synchrotron x-ray study of the first- and second- harmonic order parameter and critical fluctuation scattering at a nematic-smectic-A_2 transition in two samples of
4′-n-heptyloxy-carbonylphenyl-4′- (4″-cyanobenzoyloxy) benzoate (7APCBB). For

the first sample, the critical exponent values of the fundamental order parameter β, smectic susceptibility γ and correlation lengths $\nu_{||}$, $\nu_{\perp}$ are found to be $\beta_1 = 0.39 \pm 0.04$, $\gamma_1 = 1.34 \pm 0.14$, $\nu_{||1} = 0.70 \pm 0.07$, $\nu_{\perp 1} = 0.64 \pm 0.07$; the critical exponent values of the second harmonic are $\beta_2 = 0.76 \pm 0.04$, $\gamma_2 = 0.41 \pm 0.09$, $\nu_{||2} = 0.31 \pm 0.04$ and $\nu_{\perp 2} = 0.23 \pm 0.04$. For the second sample, the corresponding critical exponents are $\gamma_1 = 1.09 \pm 0.24$, $\nu_{||1} = 0.60 \pm 0.18$, $\nu_{\perp 1} = 0.46 \pm 0.12$ for the first harmonic and $\gamma_2 = 0.36 \pm 0.15$, $\nu_{||2} = 0.30 \pm 0.13$, $\nu_{\perp 2} = 0.22 \pm 0.10$ for the second harmonic. The results of the experiment for the second sample which had a significant drift in T_c largely confirm the results for the first sample within the experimental errors. β_1, γ_1, $\nu_{||1}$, $\nu_{\perp 1}$, β_2, and γ_2 are in good agreement with 3D XY multicritical scaling theroy which states that $\gamma_{XY} = 1.316 \pm 0.002$, $\nu_{||XY} = \nu_{\perp XY} = 0.669 \pm 0.001$, $\gamma_2 = 0.31 \pm 0.14$, $\beta_1 = 0.346 \pm 0.001$ and $\beta_2 = 0.83 \pm 0.07$. However, the critical exponents for the second harmonic correlation lengths($\nu_{||2}$, $\nu_{\perp 2}$) disagree markedly with the prediction of current theory for density wave systems.

Thesis Supervisor: Robert J. Birgeneau
Title: Cecil and Ida Green Professor of Physics Dean of Science

Acknowledgments

First and foremost, I would like to thank Bob Birgeneau for his continuous guidance and support throughout my graduate research life. His enthusiasm toward physics and the quickness to grasp the essence of a physical problem will always remain a legend to me.

I am indebted a great deal to Mike Young. We have worked closely ever since I joined the group. He introduced me to the liquid crystal field and taught me a lot about x-ray scattering. We also chatted a lot about other fun stuff besides physics, especially language. With his help, my spoken English has been improved tremendously.

I would like to thank the brothers Paul and Nathan Belk. Paul is my first year classmate. He offered me great friendship when I first arrived in the United States. His friendship makes my life in a foreign country easier. Nathan is an expert in machinery. He always gave me valuable advice and often direct hands-on help when I was doing machining.

I would like to express my appreciation to my fellow graduate students and post-docs in our research group. I vividly remembered Bill Nuttall's amusing British accent and his funny talk. John Hill was quiet but he never failed to answer my various questions. I enjoyed the girl's talk with Q. J. Harris. Martin Greven likes to tease people but very pleasantly. Barry Wells does a good job as a post-doc. He wins authority in our group. Qiang Feng is a chinese guy so we can sometimes communicate in our native language. Young Lee is the newest in our group but his technical skill struck me already. I thank him for his valuable help in Brookhaven.

Carl Garland who is the professor in Chemistry Department and his postdoc Lei Wu collaborated with us on the experiments which eventually led to this thesis. Their contribution to the success of the experiments cannot be over estimated. I worked

closely with Lei Wu in the early stage of the experiments and benefitted a great deal from his experience.

Finally, I would like to thank my family. They enjoyed every tiny success I have achieved in my life. It is to them that this thesis is dedicated.

Contents

List of Figures

Chapter 1

Introduction

The states of condensed matter have two extremes. One is crystalline solids, in which atoms form a perfectly periodic array that extends to infinity in three dimensions. Another extreme is fluids or glasses, in which the atoms or molecules are completely disordered and the system is both orientationally and positionally isotropic.

However, scientists have discovered an intermediate state of matter, which is called liquid crystal. In such a state the atoms or molecules maybe distributed randomly, as in a fluid or glass, but the system is orientationlly anisotropic on a macroscopic scale, as in a crystalline solid.

The last several decades have enjoyed an intensive investigation of liquid crystals [1, 2]. The physical behavior of liquid crystals is so rich and subtle that it remains a fascinating aspect in the phase transition problem. Some fundamental issues are still unknown. As Pierre Gilles de Gennes [3] said in "the Physics of Liquid Crystals",

> *"Liquid Crystals are beautiful and mysterious; I am fond of them for both reasons."*

With our interest in understanding liquid crystals phase transitions, we will emphasize here the critical behavior of higher harmonics in the ordered phase of sine-wave order parameter systems and the tool for studying it, that is, x-ray scattering. A theory for the critical behavior of these higher harmonics has been developed in the context of hexatic liquid crystals [4, 5]. This theory describes the successive harmonics of the orientational order observed experimentally in hexatic phase transtions very well. We will come to this theory shortly. See Section 1.2 below.

This thesis concerns a high resolution x-ray scattering study of the order parameter and critical fluctuations associated with the first and second harmonics at the N-Sm-A_2 transition in the polar thermotropic liquid crystal material 4$'$-n-heptyloxy-carbonylphenyl-4$'$- (4$''$-cyanobenzoyloxy) benzoate (7APCBB). Experimental details and results are presented later in Chapter 3 and 4.

1.1 Liquid Crystals

Liquid crystals are generally classfied as nematic, cholesteric and smectic [2]. See Fig. 1-1. According to the chronological order of their discovery, smectics are labeled as A, B, C, ... I phases. It turns out to be more useful to distinguish liquid crystals by their underlying symmetry.

To talk about the symmetry of liquid crystals quantitatively, a density function $\rho(\vec{r})$ is used. $\rho(\vec{r})d^3\vec{r}$ gives the probablity of finding an atom in a volume $d^3\vec{r}$ at point $\vec{r}$. In fluids $\rho(\vec{r})$ is a constant. In crystalline solids $\rho(\vec{r})$ is anisotropic and has a long-range periodicity. If the density is anisotropic in materials that have no traditional three-dimensional long-range periodicity, these materials are liquid crystals.

1.1.1 Nematic Liquid Crystals

Liquid crystals are usually composed of long rod-like organic molecules. These molecules can have long-range molecular orientational order, which gives a natural way to achieve an anisotropic density. The nematic phase is the simplest phase

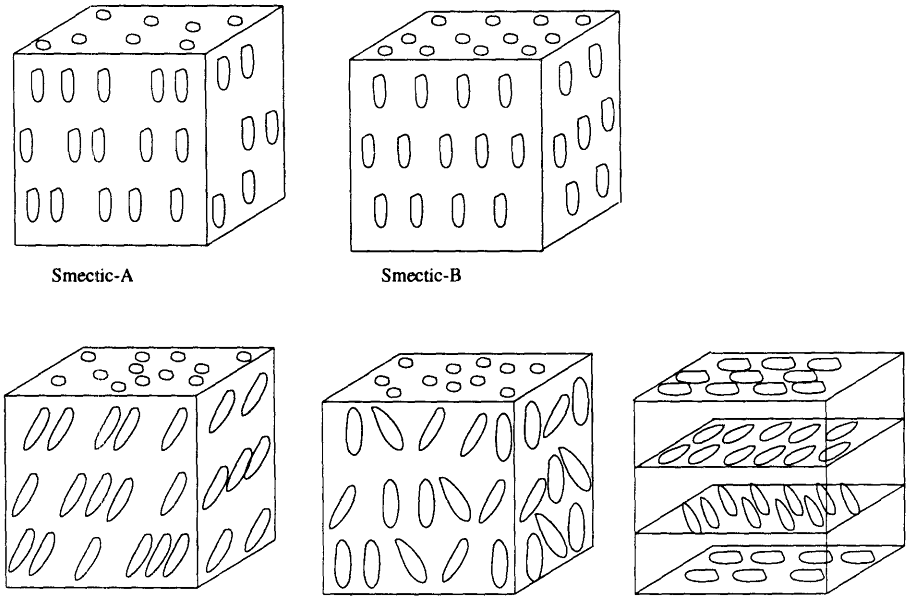

Smectic-A Smectic-B

Smectic-C Nematic Chloesteric

Figure 1-1: Common types of liquid-crystal ordering:nematic, smectic-A, smectic-B, smectic-C and cholesteric.

which contains only molecular orientational ordering. Nematics have one symmetry axis, called the director $\hat{n}$, and are optically uniaxial with a strong birefringence. The nematic phase has inversion symmetry and the orientational order parameter has quadrupole rather than dipolar symmetry. In a nematic phase the continuous rotational symmetry which is possessed by isotropic liquids is broken. This gives rise to the Goldstone modes that restore the isotropic symmetry broken by the establishment of the nematic order.

1.1.2 Smectic

In terms of symmetry, smectics have an intermediate degree of positional order in addition to molecular orientational order which exists in nematics.

Smectic-A and smectic-C liquid crystals are orientationally ordered fluids with one-dimensional density waves. The director is normal to the smectic layers in the smectic-A phase whereas it is at an angle θ to the layer normal in the C phase [6]. For nonpolar molecules, only one type of Smectic-A and Smectic-C exists. They are Sm-A_m and Sm-C_m. For polar molecules, a rich variety of Sm-A and Sm-C phases exist. These include monolayer phases Sm-A_1, Sm-C_1, partial bilayer phases Sm-A_d, Sm-C_d, and bilayer phases Sm-A_2, Sm-C_2 [7].

Fig. 1-2 schematically illustrates the four liquid crystalline phases we dissused earlier, with the diffraction patterns for each phase in Fig. 1-3.

It is worthwhile discussing briefly the smectic-A theory. Following [8, 9, 10, 11, 2, 12], the loss of translational invariance in the smectic-A phase is fully characterized by a single complex order parameter (i.e., the density wave) as

$$\rho(\vec{r}) = \rho_0\{1 + [\Psi e^{iq_0 z}]\} \tag{1.1}$$

where $2\pi/q_0$ is the layer spacing and $\Psi(\vec{r}) = |\Psi| e^{iq_0 u(\vec{r})}$. Here u(x,y,z) is the displace-

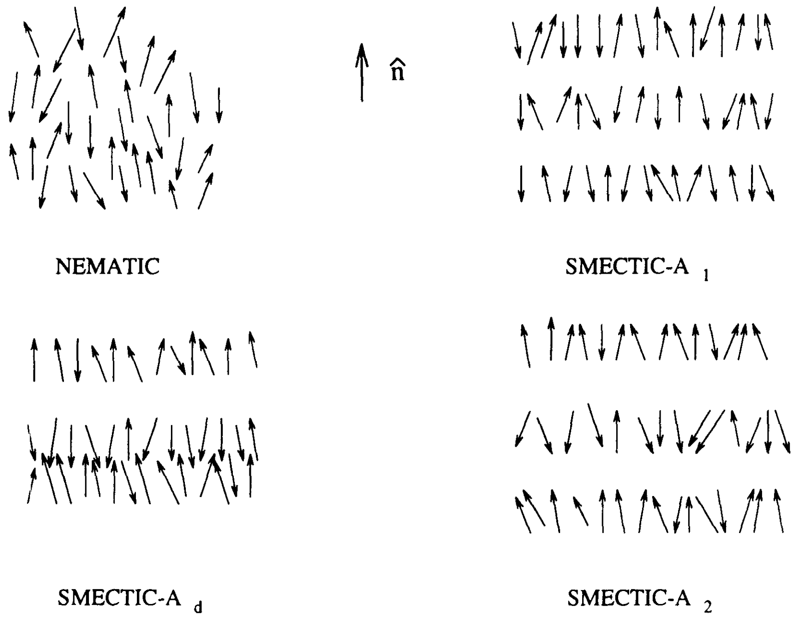

Figure 1-2: Schematic representation of the polar nematic and smectic-A phases. The molecules are drawn as thin rods with an arrow on one end to denote the lack of inversion symmetry produced by an off-center dipole.

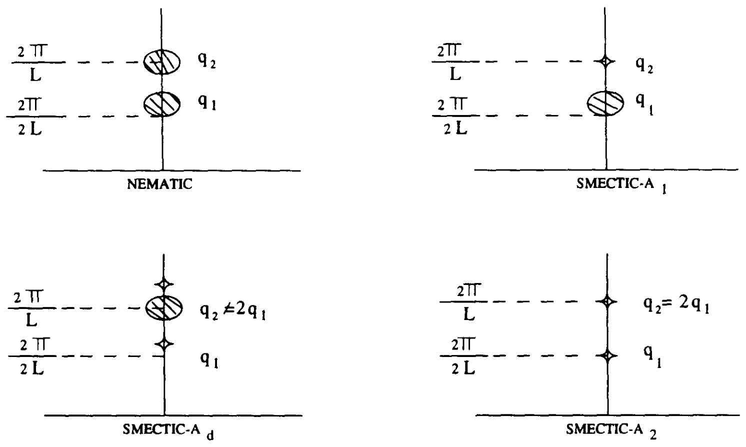

Figure 1-3: Diffraction patterns of the polar nematic and smectic-A phases. The vertical axis indicates the q_z direction and the horizontal axis indicates the $q_x q_y$ plane. The small squares denote Bragg-like spots and the large ellipses denote diffuse spots. The monolayer ordering (d = l) produces the scattering at q_2 and the dipolar ordering ($l < d \leq 2l$) produces the scattering at q_1.

ment of the layers in the z direction away from this equilibrium position. The free engergy density in **r** space is written as

$$\phi = \phi_0 + \alpha|\Psi|^2 + \frac{1}{2}\beta|\Psi|^4 + \frac{1}{2M_{||}}|\frac{\partial\Psi}{\partial z}|^2 + \frac{1}{2M_\perp} \times |(\frac{\partial}{\partial x, \partial y} + iq_0 n_{x,y})\Psi|^2 + \phi_N \qquad (1.2)$$

where the nematic free engergy is given by

$$\phi_N = \frac{1}{2}[K_1(\nabla \cdot \hat{n})^2 + K_2(\hat{n} \cdot \nabla \times \hat{n})^2 + K_3(\hat{n} \times \nabla \times \hat{n}]^2 \qquad (1.3)$$

When we Fourier transform this energy, we have the elastic energy density of the SmA elastic mode of wave vector $\vec{q}$ written as

$$F_{\vec{q}} = \frac{1}{2}(Bq_{||}^2 + Kq_\perp^4)u^2(q) \qquad (1.4)$$

where B is the compressibility for the smectic layers, K is the nematic phase splay elastic constant.

The mean-squared fluctuations $< u^2 >$ can be calculated by applying the equipartition theorem to Eq. 1.4 and summing over all wave vectors $< q_0$. One finds

$$\begin{aligned} < u^2 > &= (2\pi)^{-3}kT\int_{-q_0}^{q_0}\int_{q_{min}}^{q_{max}}(Bq_{||}^2 + kq_\perp^4)^{-1}2\pi q_\perp dq_\perp \\ &= (4\pi)^{-1}kT(BK)^{-\frac{1}{2}}\int_{q_{min}}^{q_{max}}(q_\perp^2 + \xi_M^{-2})^{-\frac{1}{2}}dq_\perp \\ &= (4\pi)^{-1}(BK)^{-\frac{1}{2}}kTln(q_{max}L/2\pi) \qquad for\ \ \xi_M = 0 \qquad (1.5) \\ &\approx (4\pi)^{-1}(BK)^{-\frac{1}{2}}kTln(2\xi_M q_{max}) \qquad for\ \ 0 < \xi_M \ll L \qquad (1.6) \end{aligned}$$

From the above derivation, we can see that the mean-squared displacement diverges logarithmically with the smaller of L or ξ_M. Consequently, a three dimensional smectic-A liquid crystal in zero magnetic field does not have true long-range positional order at any non-zero temperature. This is referred to as a Landau-Peierls instability.

In the harmonic approximation [13], the instantaneous correlations of a smectic-A liquid crystal are calculated to exhibit an anisotropic power-law dependence on the molecular separation. The x-ray scattering structure factor, which is the Fourier transform of the correlation functions, has the form of

$$S(0,0,q_{||}) \sim (q_{||} - q_0)^{-2+\eta} \tag{1.7}$$

and

$$S(q_\perp,0,q_0) \sim q_\perp^{-4+2\eta} \tag{1.8}$$

with

$$\eta = kT(q_0^2/8\pi)(BK)^{-\frac{1}{2}} \tag{1.9}$$

1.2 A Theory for the Critical Behavior of Higher Harmonics

Before our experiment, no experiments have been reported on the critical fluctuations associated with the higher harmonics of sine-wave order parameter systems. However, there were some experiments investigating the higher harmonics order parameters in the context of hexatic liquid crystals. A theory has been developed to describe the successive harmonics of the orientational order observed experimentally in hexatic phase transitions [5].

As we mentioned in 1.1, the density of liquid crystals is anisotropic. Smectic-A liquid crystals have a uniaxial orientational ordering of the molecules, and thus anisotropic quasi long-range positional order. However, there is another way to achieve anisotropic order in liquid crystal type material. It is commonly called *bond* *orientational* long-range order. A state with bond-orientational long range order may be viewed as one in which the translational ordering of the crystal lattice has been lost but the underlying orientational anisotropy of the intermolecular order remains. Fig. 1-4 illustrates this idea. Two dimensional, bond orientationally ordered systems with triangular symmetry are usually called *hexatic.*

The theoretical analysis of the phase transition from the smectic-A to hexatic phases starts with the Ginzburg-Landau Hamiltonian [14, 15]

$$\bar{H} = \int d^dx\{\frac{1}{2}|\nabla\psi_6(\vec{x})|^2 + \frac{1}{2}r|\psi_6(\vec{x})|^2 + u_4^0|\psi_6(\vec{x})|^4 + u_6|\psi_6(\vec{x})|^6 - hRe\psi_6(\vec{x})\} \quad (1.10)$$

where $\psi_6(\vec{x})$ is the local order parameter. h is the conjugate ordering field which in a smectic-C phase is determined by the average tilt order parameter, $\phi(h \sim \phi)$.

The object actually measured in an x-ray scattering experiments is

$$C_{6n} = Re < \Psi_{6n} >= Re \int_{-\frac{\pi}{6}}^{\frac{\pi}{6}} d\theta e^{i6n\theta} S(\vec{q}),$$

where $S(\vec{q})$ is the structure factor and θ is the angle between $\vec{q}$ and some reference axis. C_{6n} can be related to Equ. 1.10 by the relationship $\Psi_6 = \frac{1}{V} \int d\vec{x}\psi_6(\vec{x})$.

To study C_{6n},we add to Equ. 1.10 the field term $H_n = g_n \int d^dx Re(\psi_6^n)$. Following a standard statistical mechanical techniques, we obtain

$$C_{6n} \sim (\frac{\partial ln(Z)}{\partial g_n})_{g_n=0} \sim (\frac{\partial F}{\partial g_n})_{g_n=0} \quad (1.11)$$

Asymptotically close to the XY-model fixed point,the free energy scales as

$$f(t, g_n) = |t|^{2-\alpha} f(g_n/|t|^{\phi_n}), \quad (1.12)$$

where t is the reduced temperature, α is the XY-model heat capacity exponent

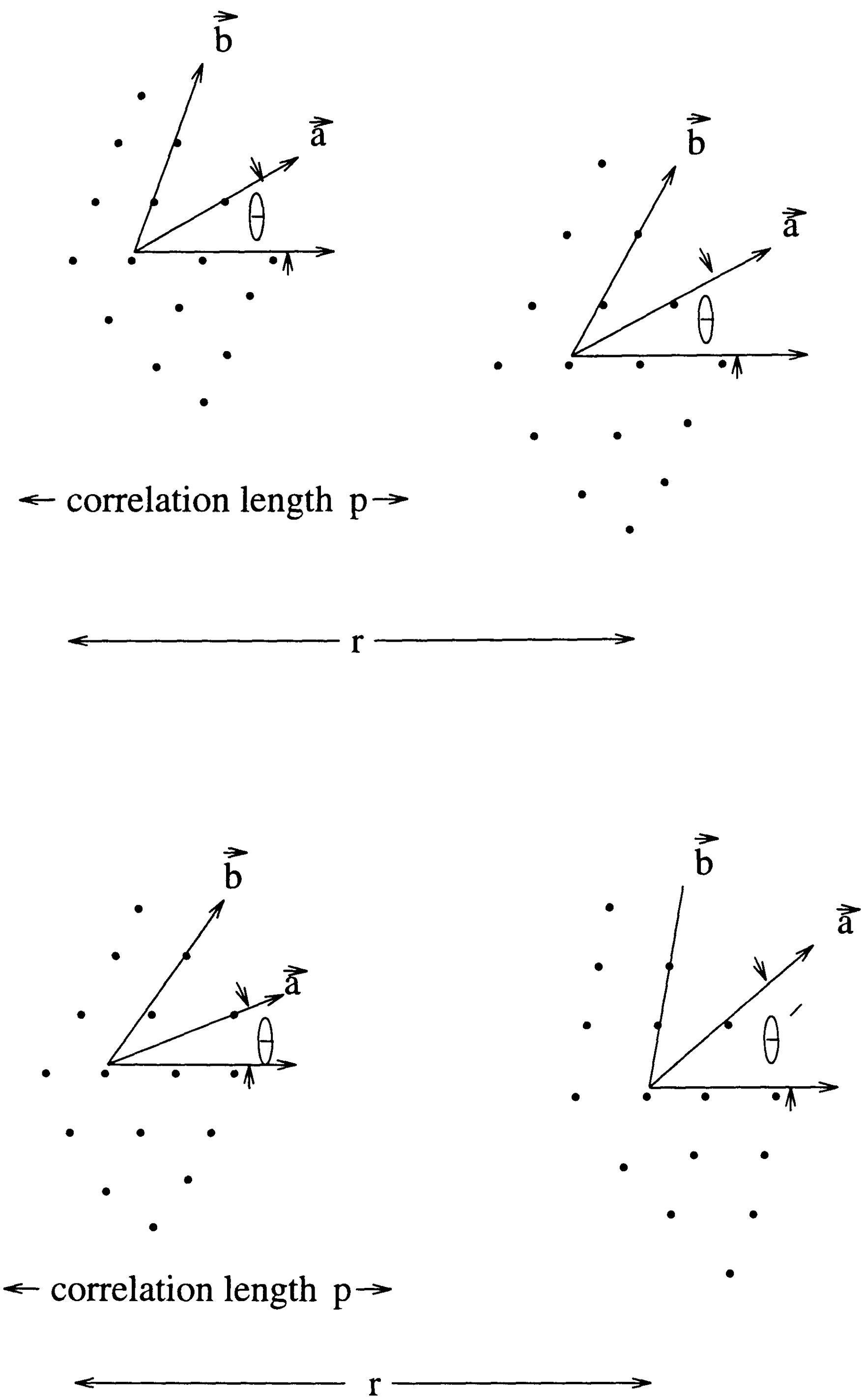

Figure 1-4: **Bond-orientational order** in a triangular two-dimensional lattice. At top, molecular positions are correlated only over a short distance p,while the orientation of the lattice vectors $\vec{a}$ and $\vec{b}$ are preserved throughout the sample. At bottom, the orientational order of the cystal axes is also only short range.

and ϕ_n is the appropriate crossover exponent [16]. Equ. 1.12 implies that

$$C_{6n} \sim |t|^{2-\alpha-\phi_n} \sim C_6^{\sigma_n}, \tag{1.13}$$

with

$$\sigma_n = \frac{2-\alpha-\phi_n}{2-\alpha-\phi_1} = \frac{2(d-\lambda_n)}{d-2+\eta} \tag{1.14}$$

where $\lambda_n = \phi_n/\nu_n$(where ν_n is the XY correlation length exponent, $\xi_n \sim |t|^{-\nu_n}$).

From Equ. 1.12, one also obtains

$$\chi_n = \frac{\partial^2 F}{\partial h_n^2} \sim |t|^{2-\alpha-2\phi_n} \sim |t|^{-\gamma_n} \tag{1.15}$$

where χ_n is the XY susceptibility for nth harmonic, γ_n is its critical exponent.

From Equ. 1.12, $f(t, g_n)$ due to fluctuations at different harmonics should all vary like $|t|^{2-\alpha}$. Conventional hyperscaling ideas lead to $2-\alpha = 3\bar{\nu}_n = (\nu_{\|n} + 2\nu_{\perp n})$ for all harmonics and thus the expectation that $\bar{\nu}_n = \nu_{XY}$ for all n.

Basically, the above equations are the most useful scaling equations so far developed. The theory works for hexatic phases very well.

Bibliography

[1] Joel D. Brock, Robert J. Birgeneau, J. David Litster and Amnon Aharony, Physics Today **July**, 52 (1989).

[2] J. D. Litster and R. J. Birgeneau, Physics Today **35**, 261 (1982).

[3] P. G. De Gennes, *The Physics of Liquid Crystals* (Clarendon, Oxford, London, 1974).

[4] A. Aharony, R. J. Birgeneau, J. D. Brock and J. D. Litster, Phys. Rev. Lett. **57**, 1012 (1986).

[5] J. D. Brock, D. Y. Noh, B. R. McClain, J. D. Litster, R. J. Birgeneau, A. Aharony, P. M. Horn, and J. C. Liang, Z. Phys. B **74**, 197 (1989).

[6] P. G. De Gennes, Mol. Cryst. Liq. Cryst. **21**, 49 (1973).

[7] Xin Wen, C. W. Garland, and G. Heppke, Physical Review A **44**, 5064 (1991).

[8] P. G. De Gennes, Sol. St. Comm **10**, 753 (1972).

[9] K. K. Kobayashi, Phys. Lett. **31A**, 125 (1970).

[10] W. McMillan, Phys. Rev. A **4**, 1238 (1971).

[11] K. K. Chan, P. S. Pershan, and L. B. Sorensen, physical Review A **34**, 1420 (1986).

[12] J. Als-Nielsen, andJ. D. Litster, Physical Review B **22**, 312 (1990).

[13] A. Caillé, C. R. Acad. Sci. Ser.B **274**, 891 (1972).

[14] S. Ostlund, and B. I. Halperin, Phys. Rev. B **23**, 335 (1981).

[15] R. Bruinsma, and D. R. Nelson, Phys. Rev. B **23**, 402 (1981).

[16] A. Aharony, C. Domb, M. S. Green, *Phase Transitions and Critical Phenomena* (Academic Press, New York, 1976).

Chapter 2

X-Ray Scattering

The x-ray scattering technique has been widely used in condensed matter experiments. Accordingly, we discuss the technique at some length in this chapter.

2.1 X-ray Sources

2.1.1 Conventional X-ray Sources

Conventional x-ray source is a vacuum tube with two electrodes maintained at a very high voltage difference. The electrons escaping from the hot filament(cathode) are accelerated under high voltage toward the target metal(anode) (Fig. 2-1) where they are stopped instantly; therefore x-ray radiation is generated. The radiation consists of the continuous and characteristic spectrum of the anode. The continuous spectrum results from the great deceleration of the electrons. It is usually referred to as Bremsstrahlung radiation [1].The characteristic x-rays are obtained when the core electrons of the anode are hit by the bombarding electrons. We all know from basic quantum mechanics that the energy is quantized in the atom. The atomic energy level is distinguished by labels K, L, M..., corresponding to the ground state, first

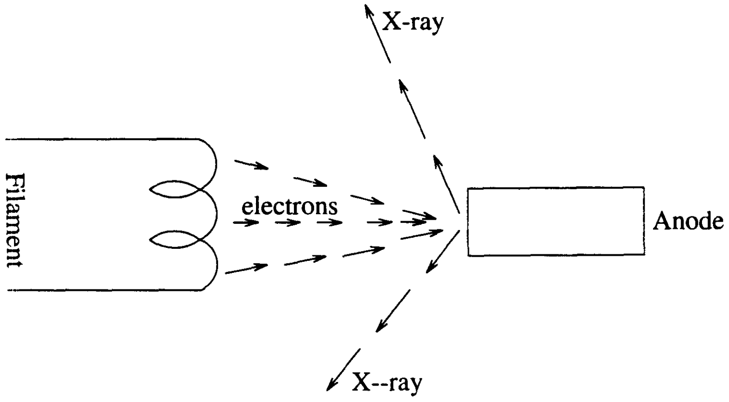

Figure 2-1: conventional x-ray source: anode.

excited state, second excited state... of the atom. If the bombarding electrons move enough energy to the core electrons, the core electrons are excited to higher energy states leaving vacancies which will be filled immediately by electrons from an outer shell. Characteristic x-rays are emitted from the target metal when the electrons make transitions from an outer shell to a vacant inner shell as shown in Fig. 2-2. These characteristic x-rays are very sharply peaked in energy with a width determined by the lifetime of the atomic states involved in the transition, and is usually less than 10eV.

Conventional x-ray sources fall into two main categories: fixed anode and rotating anode. We are more interested in the rotating anode because in a rotating anode machine, the heat generated by the electron bombardment is dissipated more efficiently than in a fixed anode configuration by allowing the anode to rotate rapidly while cooling water circulate through its interior. Thus higher x-ray power can be achieved. In our group, we have one 18kw Rigaku rotating anode machine.

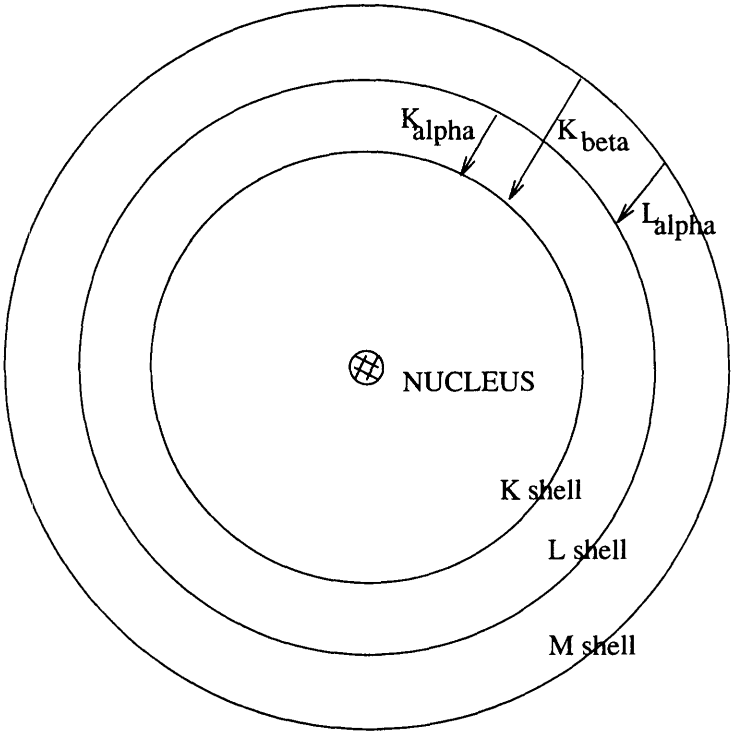

Figure 2-2: Electronic transition from one atomic state to another. Emission processes are indicated by arrows.

2.1.2 Synchrotron Radiation

The radiation emitted by an extremely relativistic charged particle under an instantaneous circular motion is called synchrotron radiation (**SR**). The energy and angular distribution of **SR** from a single electron moving with constant velocity v in a circular orbit, is given by [2]

$$I(\lambda, \Psi) = \frac{27}{32\pi^3} \frac{e^2 c}{R^2} (\frac{\lambda_c}{\lambda})^4 \gamma^8 [1 + (\gamma\Psi)^2]^2 \{K^2_{\frac{2}{3}}(\xi) + \frac{(\gamma\Psi)^2}{1 + (\gamma\Psi)^2} K^2_{\frac{1}{3}}(\xi)\} \qquad (2.1)$$

with $\lambda_c = \frac{4\pi R}{3}\gamma^{-3}$ and $\xi = \frac{\lambda_c}{2\lambda}[1 + (\gamma\Psi)^2]^{\frac{3}{2}}$. $K_{\frac{1}{3}}$ and $K_{\frac{2}{3}}$ are modified Bessel functions of the second kind.

SR sources have outstanding advantages compared to conventional x-ray sources in the following characteristics:

- A continous spectrum from the infrared to the x-ray region
- High collimation of the radiation in the direction perpendicular to the plane of the orbit ($\sim$ 1mrad)
- High flux of the radiation (10^{12} photons/sec)

A **SR** source consists of two main parts. Namely, the storage ring which has various facilities to guide the very high energy (of the order of a few GeV) electrons in a stable orbit, and the beam line which controls the resulting x-rays from the storage ring to the user(hutch).

Most of the data presented in this thesis were obtained utilizing X-20 MIT-IBM beam line at the National Synchrotron Light Source at Brookhaven National Lab. We use **SR** instead of the $Cu - K_\alpha$ radiation from the rotating anode facility in M.I.T. because the $Cu - K_\alpha$ x-ray flux is too weak to be used in measuring the second harmonic fluctuations in the nematic phase; only the **SR** source can give us satisfactory intensity.

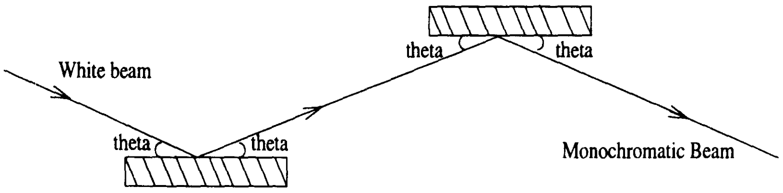

Figure 2-3: Configuration of the Monochromator Crystals.

The beam line consists of long stainless steel pipes maintained at high vacuum ($10^{-9} - 10^{-7}$). Shield walls and lead blocks are installed to stop high energy particles and radiation. A double bounce monochromator (Fig. 2-3) is used to select a narrow band of energies from the continuous-spectrum x-ray beam. In X-20b, a fixed energy of 17.4KeV is commonly used.

2.2 X-ray Scattering Theory

2.2.1 Classical Treatment

A good reference book is [3].

The x-ray scattering process can be classically thought about as the radiation from an accelerating charge due to the time varying electric field provided by the x-ray. For elastic scattering, the differential cross section is

$$\frac{\partial P}{\partial \Omega} = \frac{c}{8\pi} E_0^2 \frac{e^4}{m^2 c^4 R^2} \left(\frac{1 + cos^2\phi}{2}\right) \tag{2.2}$$

where $\frac{1+cos^2\phi}{2}$ is the polarization factor.

When considering the x-ray scattering from a three dimensional finite size crystal, coherence must be considered. Besides the factor in the left hand of Equ. 2.2, the whole differential cross section has a additional factor $F\frac{sin^2(\pi/\lambda)(\vec{s}-\vec{s_0})\cdot N_1\vec{a_1}}{sin^2(\pi/\lambda)(\vec{s}-\vec{s_0})\cdot\vec{a_1}}\frac{sin^2(\pi/\lambda)(\vec{s}-\vec{s_0})\cdot N_2\vec{a_2}}{sin^2(\pi/\lambda)(\vec{s}-\vec{s_0}\cdot\vec{a_2}}\frac{sin^2(\pi/\lambda)(\vec{s}-\vec{s_0})\cdot N_3\vec{a_3}}{sin^2(\pi/\lambda)(\vec{s}-\vec{s_0})\cdot\vec{a_3}}$. where F is the structure factor of the crystal and the cystal has the shape of a parallelopiped with edges $N_1\vec{a_1}, N_2\vec{a_2}, N_3\vec{a_3}$ parallel to the crystal axes $\vec{a_1}, \vec{a_2}, \vec{a_3}$.

Consequently, the directions at which you can get maximum intensity satisfy the three Laue equations:

$$(\pi/\lambda)(\vec{s}-\vec{s_0})\cdot\vec{a_1} = h'\pi \tag{2.3}$$

$$(\pi/\lambda)(\vec{s}-\vec{s_0})\cdot\vec{a_2} = k'\pi \tag{2.4}$$

$$(\pi/\lambda)(\vec{s}-\vec{s_0})\cdot\vec{a_3} = l'\pi \tag{2.5}$$

where h', k', l' are the three integers, and $\vec{s}$, $\vec{s_0}$ are the unit vectors in the direction of the outcoming beam and incident beam respectively.

2.2.2 Quantum Treatment

Electrons in an electromagnetic field can be described by an interaction Hamiltonian between the electrons and the field. The Hamiltonian for electrons in a field is,

$$\begin{aligned} H &= \sum_j \frac{1}{2m}(\vec{p_j} - \frac{e}{c}\vec{A}(\vec{r_j}))^2 + \sum_{i,j} V(\vec{r_{i,j}}) - \frac{e\hbar}{2mc}\sum_j \vec{S_j}\cdot\nabla\times\vec{A}(\vec{r_j}) \\ &\quad -\frac{e\hbar}{2mc}\sum_j \vec{S_j}\cdot\{\vec{E}(\vec{r_j})\times(\vec{p_j} - \frac{e}{c}\vec{A}(\vec{r_j}))\} \\ &\quad +\sum_{\vec{k},\lambda}\hbar\omega_{\vec{k}}(C^+(\vec{k},\lambda)C(\vec{k},\lambda) + \frac{1}{2}) \end{aligned} \tag{2.6}$$

where i, j represent the electrons and $C^+(\vec{k},\lambda), C(\vec{k},\lambda)$ is the creation and annihilation operator for a photon with wave vector $\vec{k}$ and polarization λ. The Hamiltonian is conveniently factorized into three parts,

$$H = H_e + H_R + H_{int} \tag{2.7}$$

where

$$\begin{aligned}
H_e &= \sum_j \frac{\vec{P}_j^2}{2m} + \sum_{i,j} V(\vec{r}_{i,j}) + \frac{e\hbar}{2(mc)^2} \sum_j \vec{S}_j \cdot (\nabla\Psi \times \vec{P}_j) \\
H_R &= \sum_{\vec{k},\lambda} \hbar\omega_k (C^+(\vec{k},\lambda)C(\vec{k},\lambda) + \frac{1}{2}) \\
H_{int} &= \frac{e^2}{2mc^2} \sum_j \vec{A}(\vec{r}_j)^2 - \frac{e}{mc} \sum_j \sum_j \vec{A}(\vec{r}_j) \cdot \vec{P}_j \\
&\quad - \frac{e\hbar}{mc} \sum_j \vec{S}_j \cdot [\nabla \times \vec{A}(\vec{r}_j)] \\
&\quad - \frac{e\hbar}{2(mc^2)} \frac{e^2}{c^2} \sum_j \vec{S}_j \cdot [\dot{\vec{A}} \times \vec{A} - \frac{c}{e} \dot{\vec{A}} \times P - c\nabla\phi \times \vec{A}]
\end{aligned}$$

The interaction hamiltonian responsible for the scattering process is part of H_i:

$$H_I = \frac{e^2}{2mc^2} \int d\vec{r} \rho(\vec{r}) \vec{A}^2(\vec{r}) + \frac{e}{mc} \int d\vec{r} \rho(\vec{r}) \vec{A}(\vec{r}) \cdot \vec{P} \tag{2.8}$$

Quite generally we have the following formula:

$$\frac{d\sigma}{d\Omega dE} = \frac{W_{i \to f}}{IncidentFlux} \tag{2.9}$$

By Fermi's golden rule, the transition probability $W_{i \to f}$ is

$$\begin{aligned}
W_{i \to f} &= \frac{2\pi}{\hbar} \rho(E) \delta(E_B - E_A - \hbar(\omega_f - \omega_i)) \\
&\quad | < \vec{k}_f, \vec{e}_f, B | H_I | \vec{k}_i, \vec{e}_i, A > \\
&\quad + \sum_{i,\pm} \frac{< \vec{k}_f, \vec{e}_f, B | H_I | I >< I | H_I | \vec{k}_i, \vec{e}_i, A >}{E_I - E_A \pm \hbar(\omega_f - \omega_i)} |^2
\end{aligned} \tag{2.10}$$

where $\rho(E)$ is the density of states.

With the help of the second quantization [4], after a complicated calculation, one finally obtains the scattering cross section as

$$
\begin{aligned}
\frac{d\sigma}{d\Omega dE} &= (\frac{\omega_f}{\omega_i}) r_0^2 |\vec{\epsilon_i} \cdot \vec{\epsilon_f} \sum_{|B>} < B| \int d\vec{r} \rho(\vec{r}) e^{i\vec{q}\cdot\vec{r}} |A > \\
& - \sum_I \int d\vec{r} \rho(\vec{r}) \{ \frac{< B|\vec{P} \cdot \vec{\epsilon_f}|I >< I|\vec{P} \cdot \vec{\epsilon_i}|A >}{E_I - E_A + \hbar\omega} \\
& + \frac{< B|\vec{P} \cdot \vec{\epsilon_i}|I >< I|\vec{P} \cdot \vec{\epsilon_f}|A >}{E_I - E_A + \hbar\omega} \} |^2 \\
& \delta(E_B - E_A + \hbar\omega)
\end{aligned}
\tag{2.11}
$$

where $r_0 = \frac{e^2}{mc^2} = 2.82 \times 10^{-13} cm$ is the classical electronic radius.

In the case of x-rays, for which the energy is typically much higher than the atomic binding energy, Equ. 2.11 can be simplified to

$$
\begin{aligned}
\frac{d\sigma}{d\Omega dE} &\approx (\frac{\omega_f}{\omega_i}) r_0^2 |\vec{\epsilon_i} \cdot \vec{\epsilon_f}|^2 \sum_{|B>} | < B| \int d\vec{r} \rho(\vec{r}) e^{i\vec{q}\cdot\vec{r}} |A > |^2 \delta(E_B - E_A + \hbar\omega) \\
& (\frac{k_f}{k_i})(\frac{N}{\hbar}) r_0^2 |\vec{\epsilon_f} \cdot \vec{\epsilon_i}|^2 S(\vec{q}, \omega)
\end{aligned}
\tag{2.12}
$$

where the dynamic structure factor $S(\vec{q}, \omega)$ is

$$
S(\vec{q}, \omega) = \frac{1}{N} \sum_{|B>} \delta(\frac{E_B - E_A}{\hbar} + \omega) | < B| \int d\vec{r} e^{i\vec{q}\cdot\vec{r}} \rho(\vec{r}) |A > |^2 \tag{2.13}
$$

N is the number of electrons.

In the usual x-ray scattering experiment, the cross section is automatically integrated over energy. The static structure factor $S(\vec{q}) = \int S(\vec{q}, \omega) d\omega$ comes into use under this situation.

$$
\begin{aligned}
S(\vec{q}) &= \frac{1}{N}\sum_{|B>} \left| \int d\vec{r} e^{i\vec{q}\cdot\vec{r}} < B|\rho(\vec{r})|A > \right|^2 \\
&= \frac{1}{N}\int d\vec{r} e^{i\vec{q}\cdot\vec{r}} < A|\rho(\vec{r})\rho(\vec{o})|A > \qquad (2.14)
\end{aligned}
$$

Therefore, the static scattering cross section is given by,

$$
\frac{d\sigma}{d\Omega} = r_0^2|\vec{\epsilon_i}\cdot\vec{\epsilon_f}|^2 \int d\vec{r} e^{i\vec{q}\cdot\vec{r}} < \rho(\vec{r})\rho(\vec{0}) > \qquad (2.15)
$$

The term $< \rho(\vec{r})\rho(\vec{0}) >$ has its special name. It is called the density-density correlation function, usually denoted by $G(\vec{r})$.

Bibliography

[1] J. D. Jackson, *Classical Electrodynamics* (John Wiley & Sons, New York 1975).

[2] C. Kunz, *Synchrotron Radiation Techniques and Applications* (Springer-Verlag 1979).

[3] B. E. Warren, *X-Ray Diffraction* (Dover Publications,Inc, New York 1990).

[4] J. J. Sakuri, *Advanced Quantum Mechanics* (Addison-Wesley Publishing Co. 1967).

Chapter 3

Experimental Details

3.1 Samples

The compound 4'-n-heptyloxy-carbonylphenyl- 4'-(4''-cyanobenzoyloxy)benzoate or 7APCBB is a polar molecule with the structure

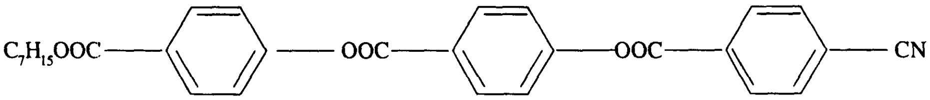

The phase-transition sequence, as determined by optical microscopy and differential scanning calorimetry [1], is

$$\mathrm{I} \underset{482\,\mathrm{K}}{\text{——}} \mathrm{N} \underset{415.8\,\mathrm{K}}{\text{——}} \mathrm{SmA}_2 \underset{412.9\,\mathrm{K}}{\text{——}} \mathrm{SmC}_2$$

The Sm-A_2 phase has a bilayer structure with layer thickness $d = 2L = 58.18\mathring{A}$, where L is the molecular length. The Sm-C_2 phase is the analogous tilted bilayer. The nematic temperature range is quite wide, which means that the McMillan ratio T_{NA}/T_{NI} is rather small(0.86). This implies that the nematic order parameter should be well saturated close to the $N-Sm-A_2$ transition; hence, this transition is expected to be second order and 3D-XY-like. This has been confirmed by a high resolution calorimetric study [2]. Analysis of $C_P(N - Sm - A_2)$data yielded the critical exponent $\alpha = -0.029$ when α was a freely adjustable parameter, and a statistically equivalent fit was obtained with α fixed at the 3D XY value ($\alpha = -0.007$).

We have studied two samples of 7APCBB. We studied the first sample in 1992 [3]. The second sample was studied in 1994. A second fresh 7APCBB sample was utilized because we wanted to exclude the possibility that the first one might have gone bad after being heated and cooled many times. Both samples were supplied by G. Heppke.

The newly arrived 7APCBB sample was white and powder-like. It was filled into a rectangular beryllium cell which was approximately 18 mm high, 10 mm long, and 2mm wide. Then the cell was heated up. The sample would melt into a smaller volume upon heating. The cell was cooled and more sample powder was filled into it. This had to be done several times until the cell was completely filled. To prevent the sample's oxidization while it was still in a high temperature state, the whole process had to be done in a gaseous nitrogen environment.

The first sample had a T_c drift of 6mK per hour. The second sample had a T_c drift of 31mK per hour. Part of the reason that the second sample had a higher T_c drift rate was that it was fresh. Specifically, the 7APCBB sample tends to have a higher T_c drift rate in the beginning.

3.2 Experimental Configuration

3.2.1 X-ray Source

Rotating Anode

The Sm-A_2 phase data were taken using the Rigaku rotating anode source at MIT in the summer of 1992. A hot filament at a large negative potential provided electrons that were focused on the anode. Electron current of 40 mAs and a potential of 30 kilovolts were selected when the data were taken. The copper $K_{\alpha 1}(\lambda_1 = 1.54056\AA)$ and $K_{\alpha 2}(\lambda_2 = 1.54439\AA)$ lines were used. An initial valence state of copper atom with a vacancy in the 1s level with a final state vacancy in the $2p_{\frac{3}{2}}$ or the $2p_{\frac{1}{2}}$ state gives rise to $K_{\alpha 1}$ and $K_{\alpha 2}$. $K_{\alpha 1}$ and $K_{\alpha 2}$ have Lorentzian energy distributions with widths of 2.66ev and 3.77ev respectively. Additionlly, there is a 1% background due to bremsstrahlung radiation.

A small fraction of the total radiation emitted from the rotating anode leaves the machine vacuum through two 1 cm Be windows on either side of the anode. The beam is controlled by an on/off electromagnetic shutter and travels to the monochromator assembly via a flight path to eliminate air scattering. The beam collimation in the scattering plane is limited by the size of the filament image on the anode and the horizontal slit S_1 in front of the monochromator. Though the filament spot is 0.5mm by 10mm,viewed at 6^o its effective size is only .5mm by 1mm. When the entrance slit separation is matched to the effective spot width(1mm), the collimation in the scattering plane is 3×10^{-3} radians HWHM. (This is for a 30 cm seperation between the anode and the monochromator entrance slit.) For a perfect monochromator cystal, i.e. no mosaic, incoming rays will be reflected in an energy range limited by the collimation, $\simeq 3 \times 10^{-3} \times 8000/tan\theta\ ev \sim 100ev$ for copper K_α x-rays. This is adequate to reject most of the bremsstrahlung and the K_β line although it is inadequate to

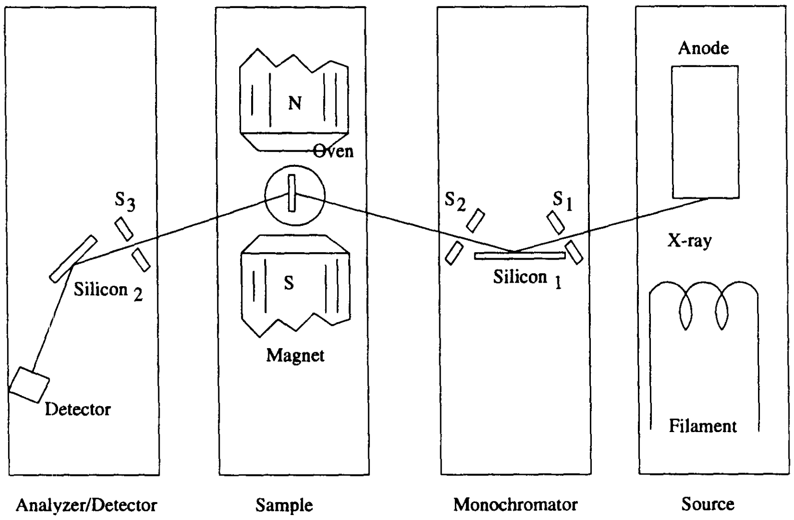

Figure 3-1: Experiment configuration: X-ray spectrometer components in the scattering plane.

separate out the $K_{\alpha 1}$ radiation from the $K_{\alpha 2}$ radiation since these lines are only 21ev apart. The horizontal exit slit after the monochromator serves only to reduce the background and is set such that it is marginally wider than the beam [4].

X-20B Synchrotron Beam Line

The experiments on nematic phase were carried out primarily on the IBM-MIT X-20B beam line at the National Synchrotron Light Source(NSLS). This beam line, equipped with a single bent Si(111) monochromator, provided a beam of x rays with energy E = 17.4 keV. Scattering was in the horizontal plane and a flat Si(111) analyzer was used to achieve high angular resolution in the scattered beam. The consequent longitudinal resolution was $3.54 \times 10^{-4} \AA^{-1}$ half-width-at-half-maximum (HWHM) for the first experiment and $5.84 \times 10^{-4} \AA^{-1}$ HWHM for the second experiment. The transverse in-plane resolution was $\simeq 10^{-5} \AA^{-1}$ HWHM in both cases. The out of plane resolution was determined by vertical collimating slits. The resulting resolution was typically $0.02\AA^{-1}$ HWHM.

3.2.2 Goniometer Assembly

The goniometer, a Huber 404, was used through out the whole experiments. It has two concentric rotation stages that can be set to an accuracy of better than .005°. These stages control the sample and the detector arm rotation. Adjustments are made such that the sample rotation is concentric with the goniometer axis via translation stages that sit on the goniometer. The entire goinometer assembly is positioned so that the x-ray beam passes through the goniometer's rotation axis.

3.2.3 Sample Alignment

Liquid crystal alignment was achieved by magnetically orienting the liquid crystal director. Both the electromagnet and the sample must ratate with the goniometer angle θ. The magnet, weighing $\sim$ 1000 pounds, is suspended from the ceiling via a hoist, a precision swivel bearing and a leaf spring. The magnet is a custom made commercial magnet manufactured by ANAC Inc., that produces a homogeneous 7 kilogauss field in a 1.6 inch gap. Fig. 3-2 shows the side view of the ANAC electromagnet. Fig. 3-3 shows the calibration curves for the ANAC magnet. When we studied the first sample, a field of 6.5 kG was achieved. 4.5 kG was used for the second sample.

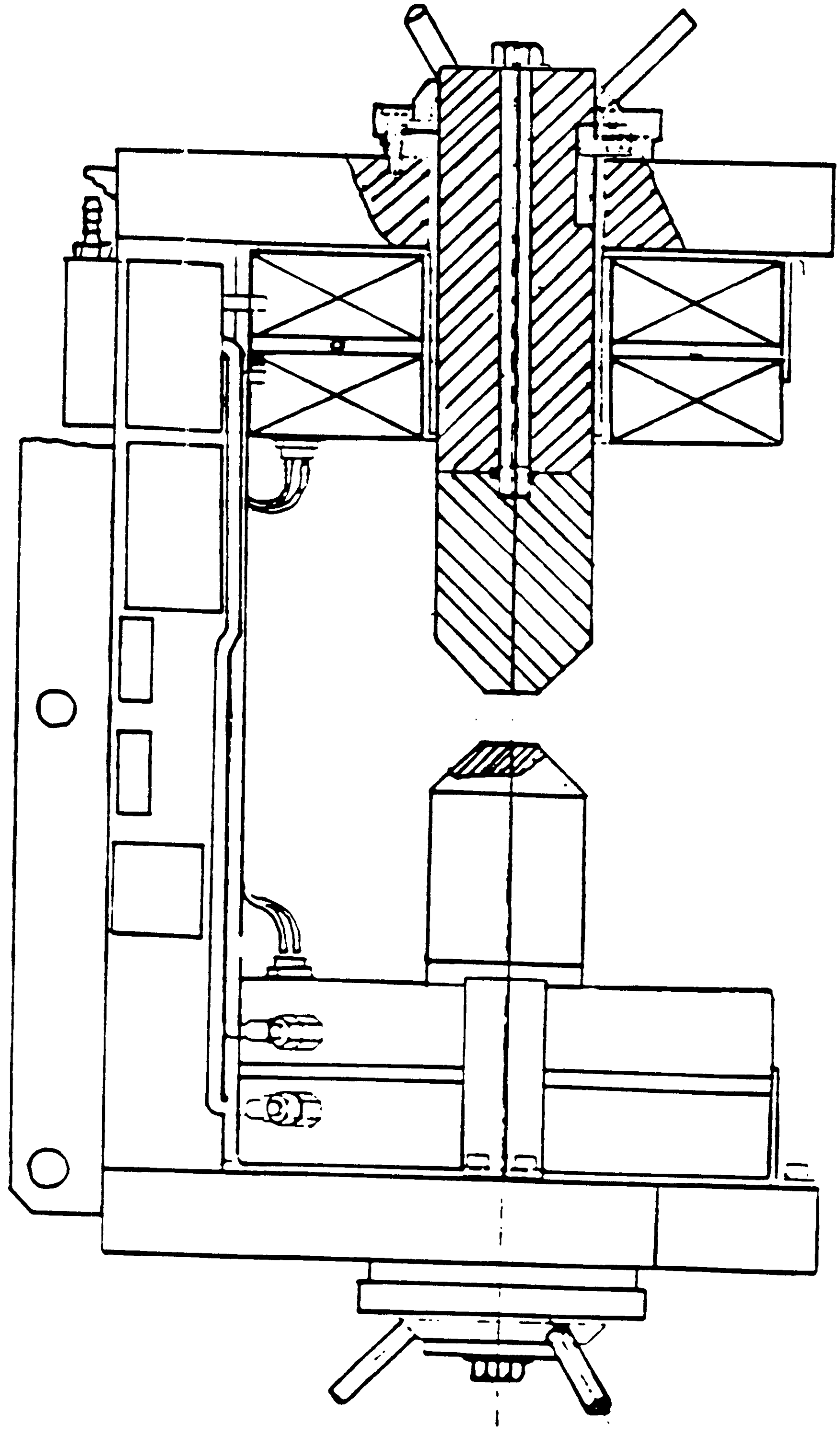

Figure 3-2: side view of the ANAC electromagnet.

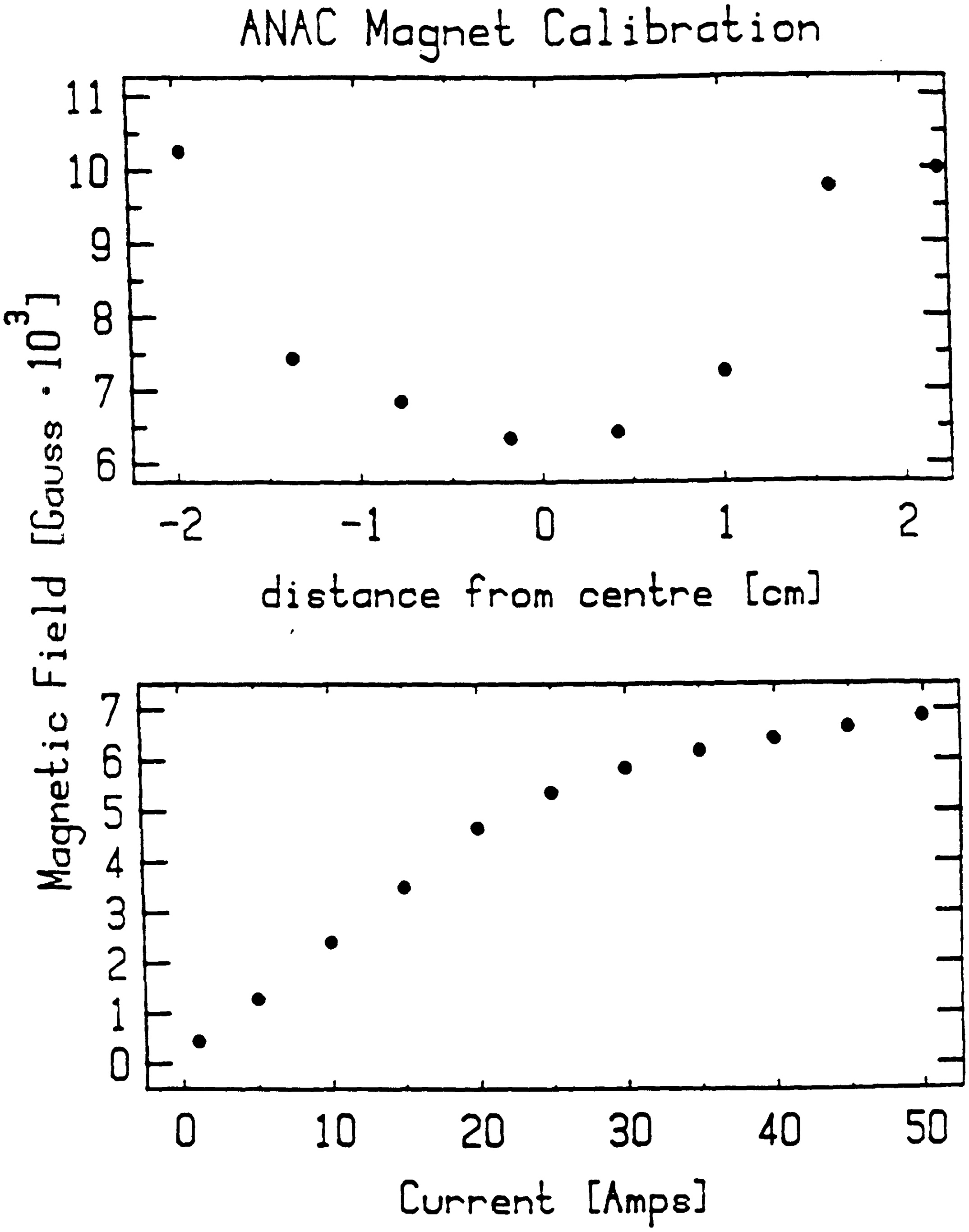

Figure 3-3: ANAC magnet calibration courtesy of Luz Martinez.
Top: Field as a function of longitudinal position.
Botton: Magnetic field as a function of magnet current.

Bibliography

[1] R. Shashidhar, K. A. Suresh, B. R. Ratna, S. Krishna Prasad, Ch. Bahr, A. Oestreicher, and G. Heppke, Mol. Cryst. Liq. Cryst. Lett **1**, 89 (1985).

[2] Xin Wen, C. W. Garland, and G. Heppke, Physical Review A **44**, 5064 (1991).

[3] Lei Wu, M. J. Young, Y. Shao, C. W. Garland, and R. J. Birgeneau, Phys. Rev. Lett. **72**, 376 (1994).

[4] B. M. Ocko, Ph.D. thesis, Massachusetts Institute of Technology, 1984.

Chapter 4

Data Analysis

We present data on the two samples of 7APCBB together with the relevant analysis.

In the nematic phase we observed two diffuse peaks at (0,0,q_0) and (0,0,2q_0) with $q_0 = 0.1080\AA^{-1}$. The experimental procedure was that a complete set of scans was carried out at both q_0 and $2q_0$ at each temperature and the temperature was then increased to the next value. Several such sweeps were done during the experiment. The value of T_c was determined frequently during the experiment by observing the onset of smectic mosaicity for the q_0 peak. Figure 4-1 shows typical scans to determine T_c for the first sample and Fig. 4-2 for the second sample.

The uncertainty in our determination of T_c was rather large for the second sample (0.004K) compared with the first one. Part of the reason is that the second sample was new and typically the T_c drifting rate is high for fresh samples. We observed a linear drift of ~ -0.006 K/h in the T_c for the first sample and a linear drift of ~ -0.031 K/h for the second sample. These effects were taken into account in the data reduction. As expected theoretically and as demonstrated in previous experiments [1], such Tc drifts have no effect on the observed critical behavior.

Fig. 4-3 shows typical longitudinal ($q_{||}$) and transverse ($q_\perp$) scans through the q_0 peak at various reduced temperatures for the first sample. Fig. 4-4 shows scans

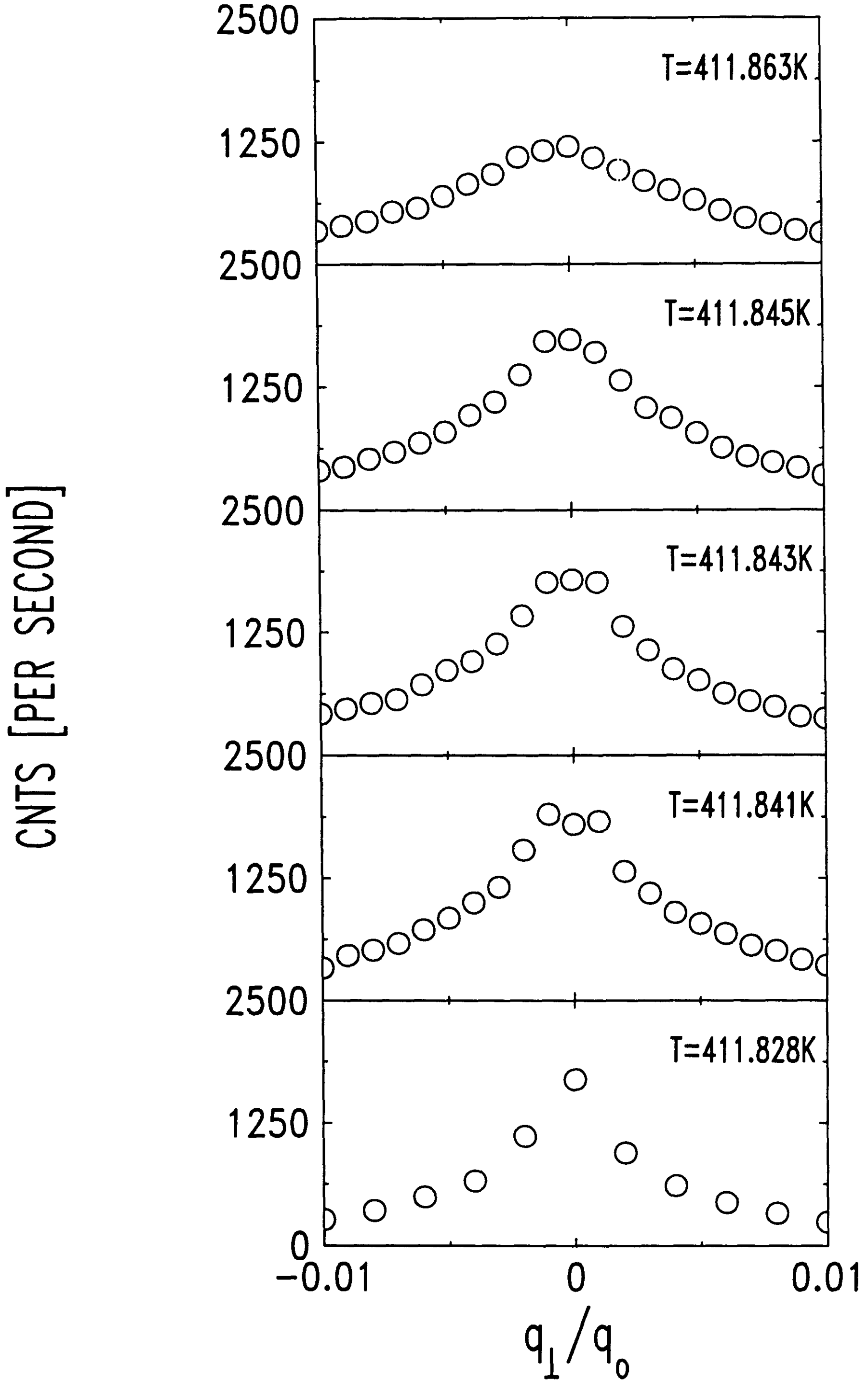

Figure 4-1: Typical T_c determination scans for the first sample. $T_c = 411.842K \pm 0.001K$.

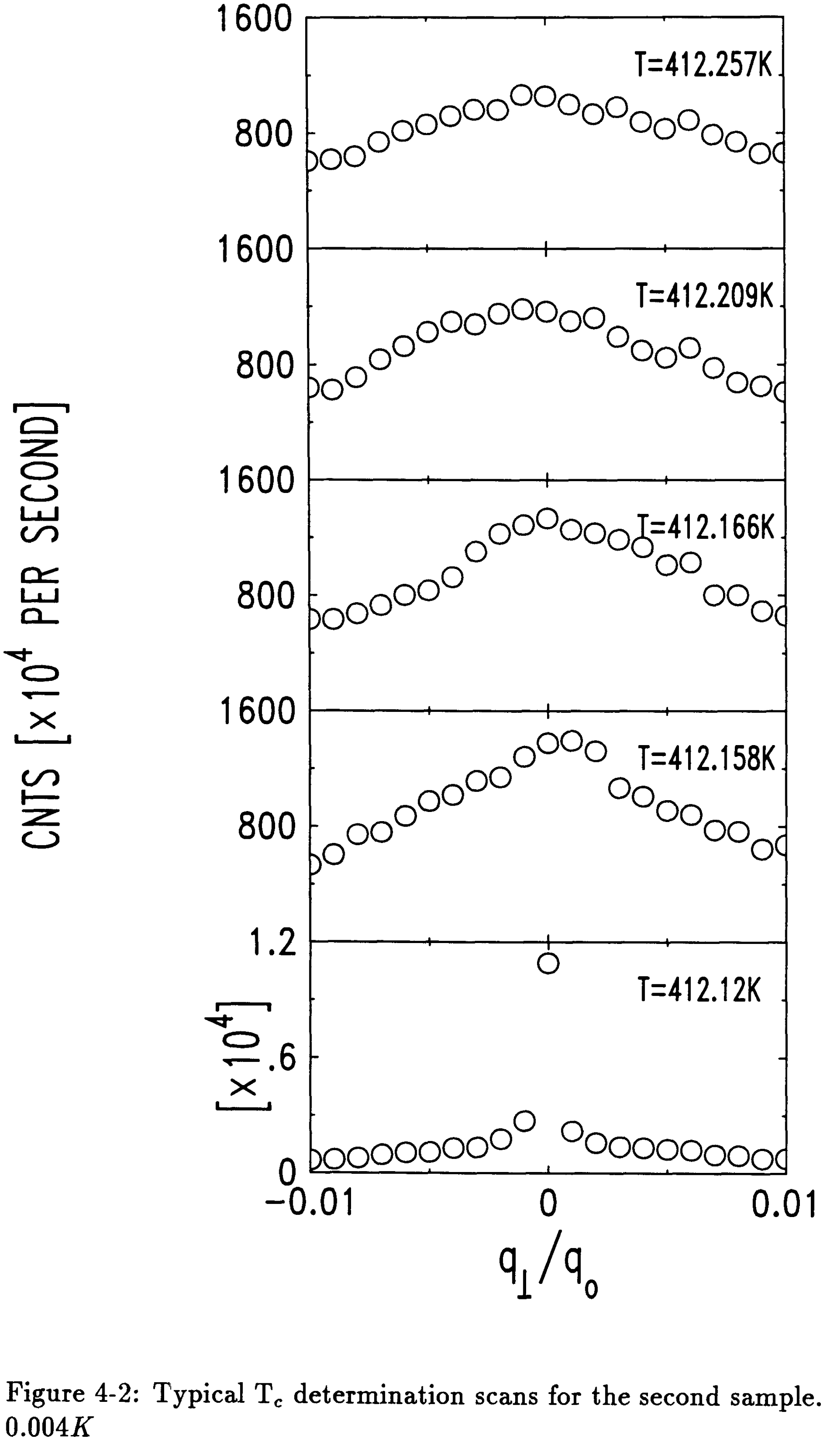

Figure 4-2: Typical T$_c$ determination scans for the second sample. $T_c = 412.162K \pm 0.004K$

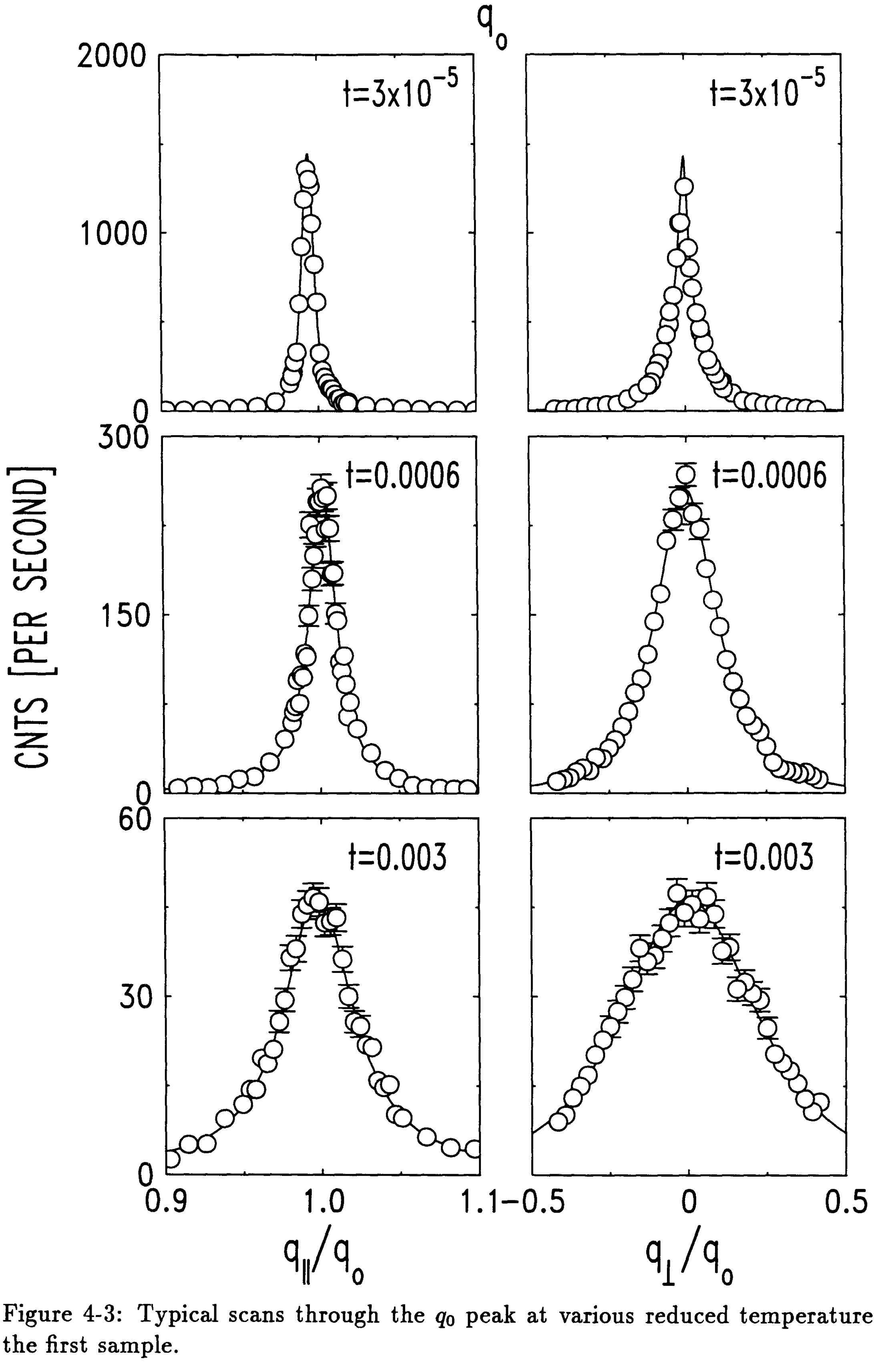

Figure 4-3: Typical scans through the q_0 peak at various reduced temperatures for the first sample.

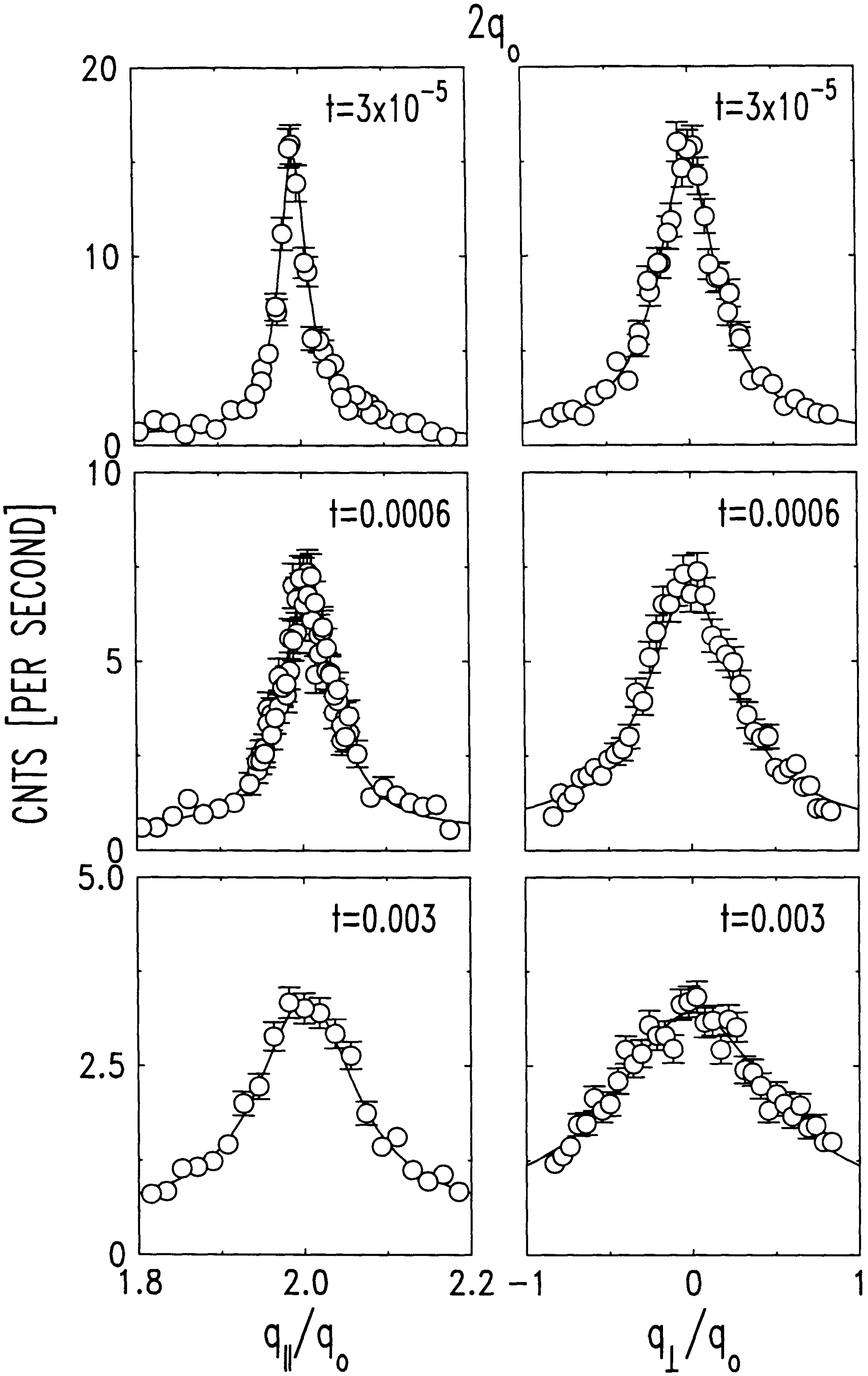

Figure 4-4: Typical scans through the $2q_0$ peak at various reduced temperatures for the first sample.

through the $2q_0$ peak for the first sample at the same reduced temperatures. Similar scans for the second sample are shown in Fig. 4-5 and Fig. 4-6.

For the first sample, the reduced temperature covered three decades (from 10^{-5} to 10^{-2}), while for the second sample, the reduced temperature covered two decades (from 10^{-4} to 10^{-2}).

From these four figures, It is evident that the difference in magnitude between the peak intensities of the q_0 and $2q_0$ scans is quite marked at all reduced temperatures with the q_0 peak much stronger. This suggests that the transition is driven by the layer formation of antiparallel dimer pairs of dipolar molecules. We now discuss our quantitative analysis of the measurements.

Above T_c, fluctuations in the components of the order parameter $\Psi_n e^{in\phi}$ give rise to critical scattering which can be described by the x-ray scattering structure factor [2]

$$S_n(\vec{q}) = \frac{k_B T \chi_n}{1 + \xi_{\|n}^2 (q_\| - nq_0)^2 + \xi_{\perp n}^2 q_\perp^2 + c_n \xi_{\perp n}^4 q_\perp^4} \tag{4.1}$$

convoluted with the instrumental resolution function. χ_n is the susceptibility and $\xi_{\|n}$ and $\xi_{\perp n}$ are the correlation lengths along respectively the longitudinal and transverse directions associated with a given order parameter $\Psi_n e^{in\phi}$. The quartic term, needed to describe the non-Lorentzian transverse line shape for the q_0 fluctuations, has a freely adjustable coefficient C_n. Fig. 4-7 shows the C_1 we obtained from the q_0 scan data for the first sample. From the figure, one can see that C_1 exhibits the same kind of temperature dependence seen typically for N-Sm-A_2 and other N-Sm-A [3] systems. The qualitative temperature dependence of C_1 can also be clearly seen in Fig. 4-8, Fig. 4-9 and Fig. 4-10. However, for the q_0 data of the second sample, we always found the fitted parameter C_1 to be zero, but with an enormous uncertainty(Fig. 4-11, Fig. 4-12, and Fig. 4-13). Therefore the two results are not

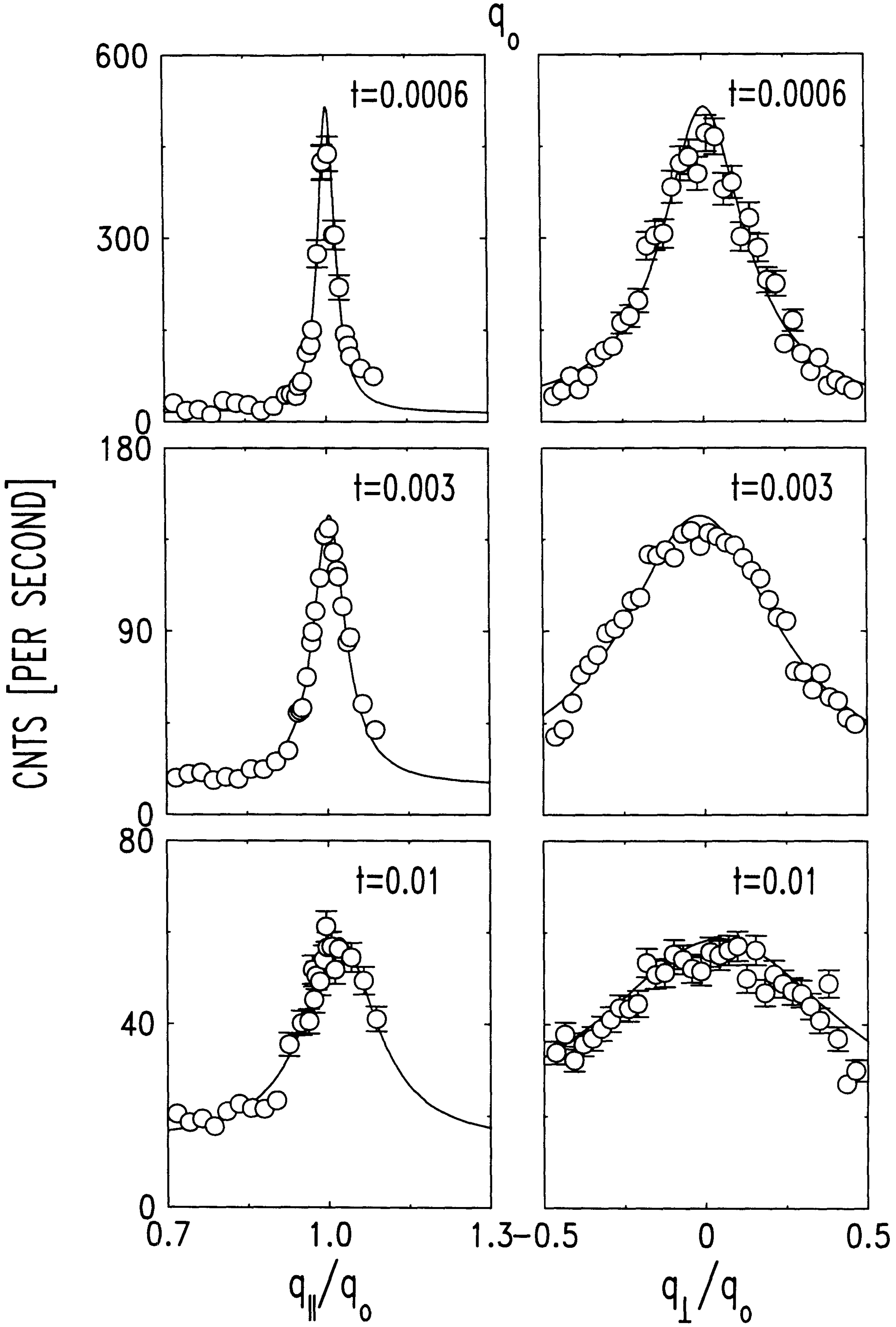

Figure 4-5: Typical scans through the q_0 peak at various reduced tempearatures for the second sample.

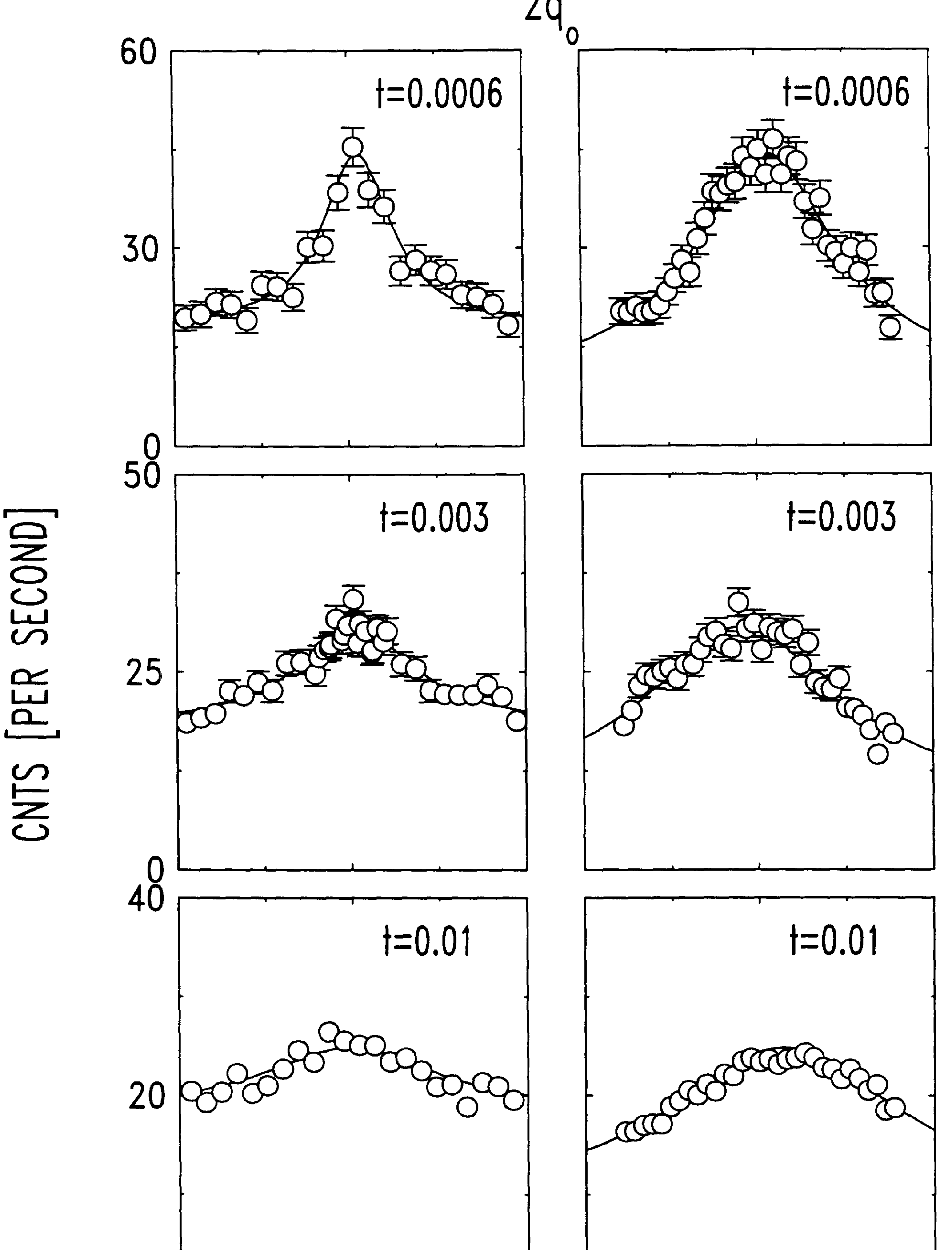

Figure 4-6: Typical scans through the $2q_0$ peak at various reduced tempearatures for the second sample.

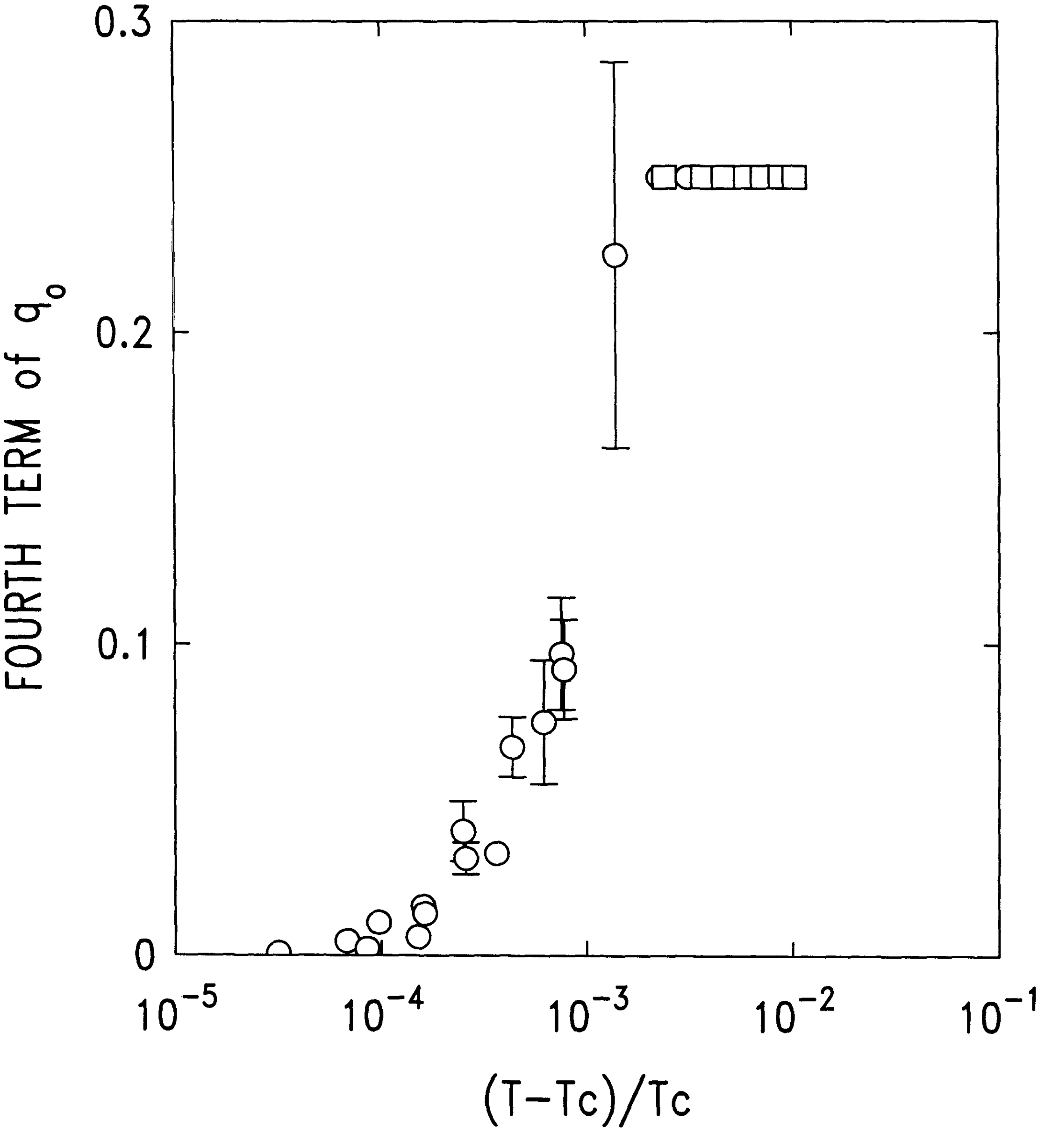

Figure 4-7: Fourth term C_1 for the first sample

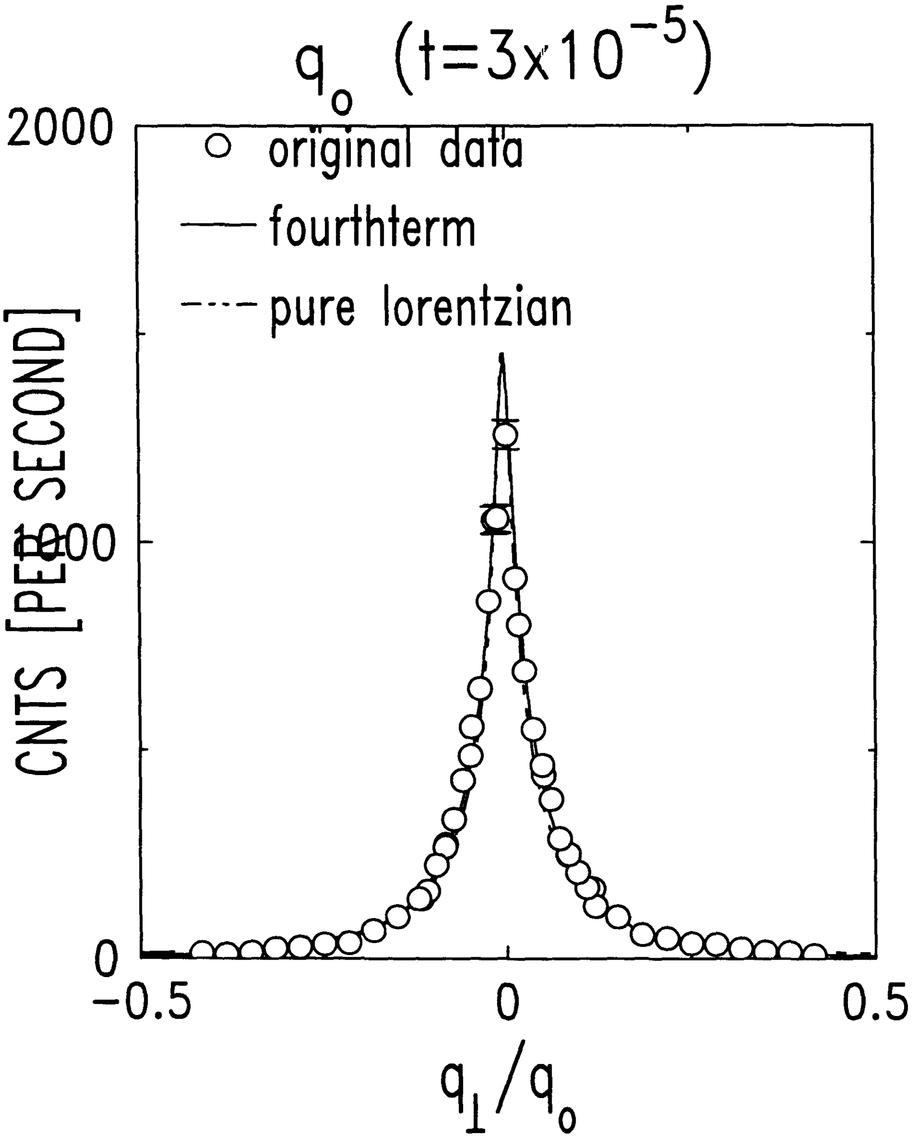

Figure 4-8: A typical transverse q_0 scan for the first sample. $t = 3\times10^{-5}$. Fourthterm fit and pure lorentzian fit have little difference, which implies C_1 is nearly zero.

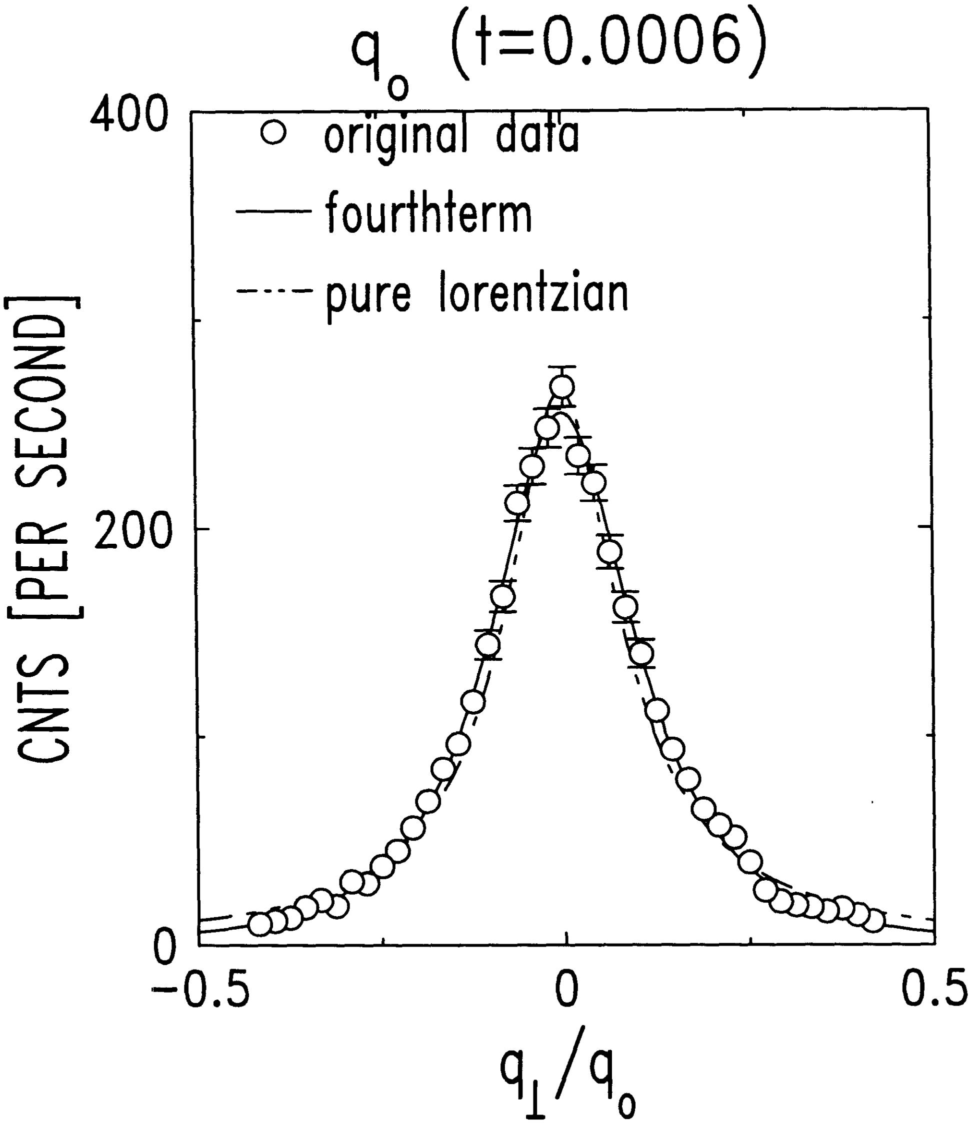

Figure 4-9: A typical transverse q_0 scan for the first sample. $t = 6 \times 10^{-4}$. Fourthterm fit and pure lorentzian fit differ slightly in the tail, which implies C_1 has a non-zero small value.

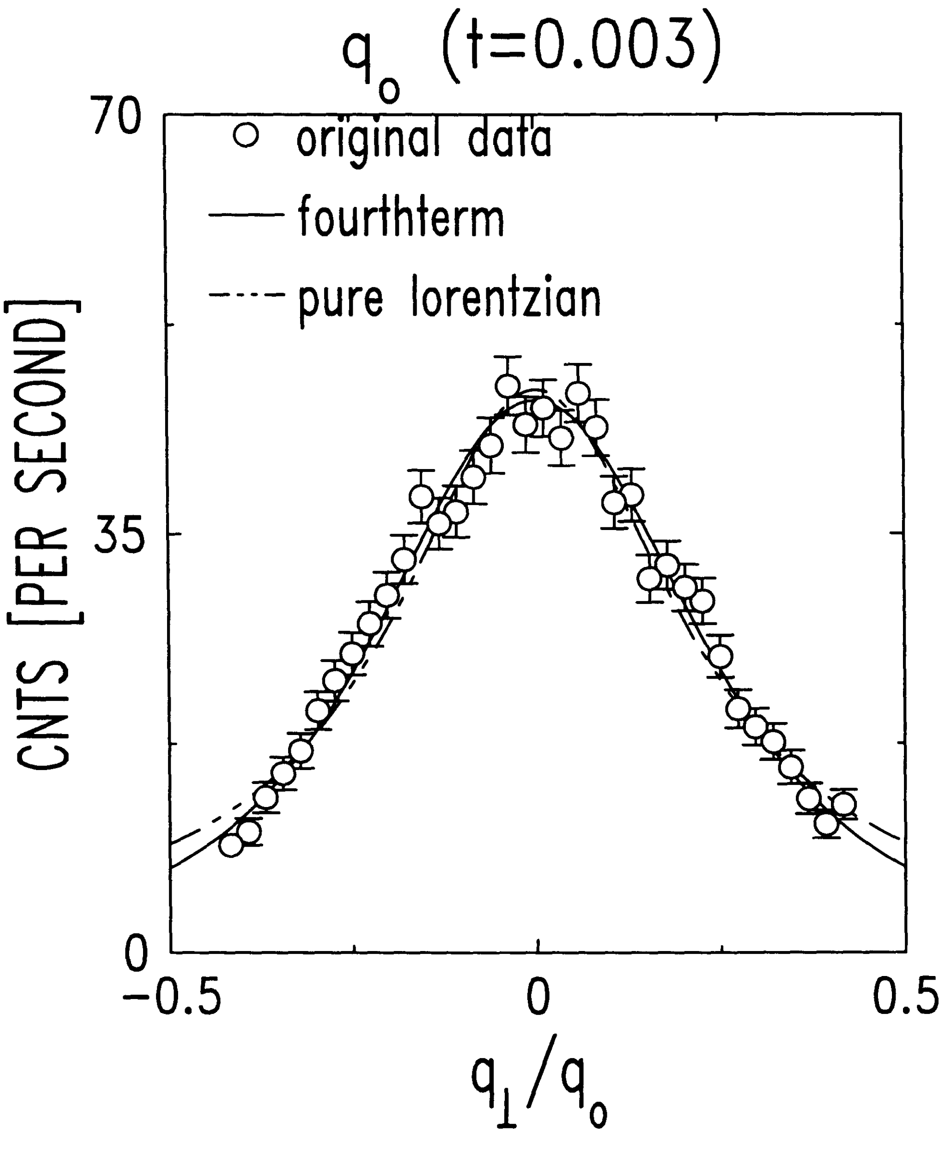

Figure 4-10: A typical transverse q_0 scan for the first sample. $t = 3\times10^{-3}$. Fourthterm fit and pure lorentzian fit differ in the tail, which implies C_1 has a non-zero value.

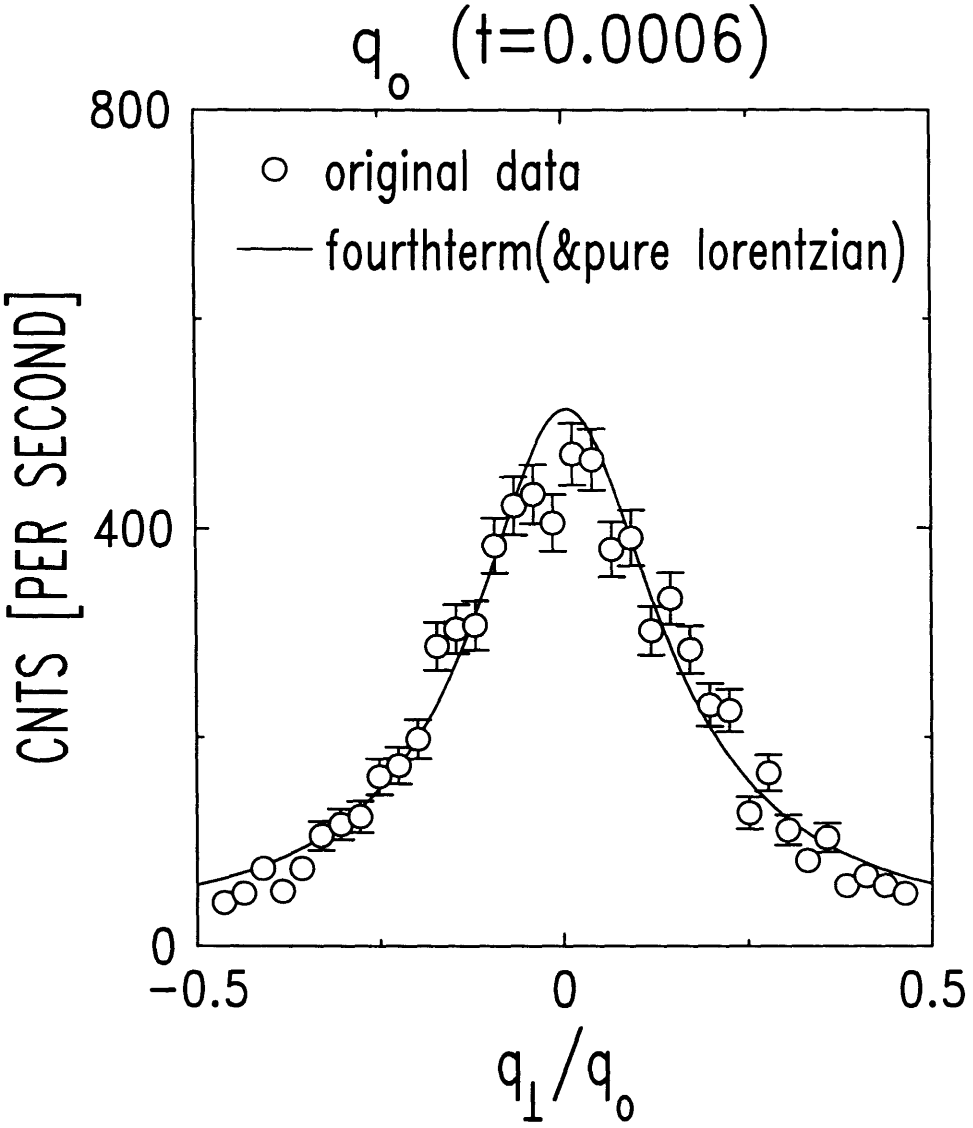

Figure 4-11: A typical transverse q_0 scan for the second sample. $t = 6\times10^{-4}$. Because the C_1 is fitted to be zero, the fourthterm fit and pure-lorentzian fit have no difference.

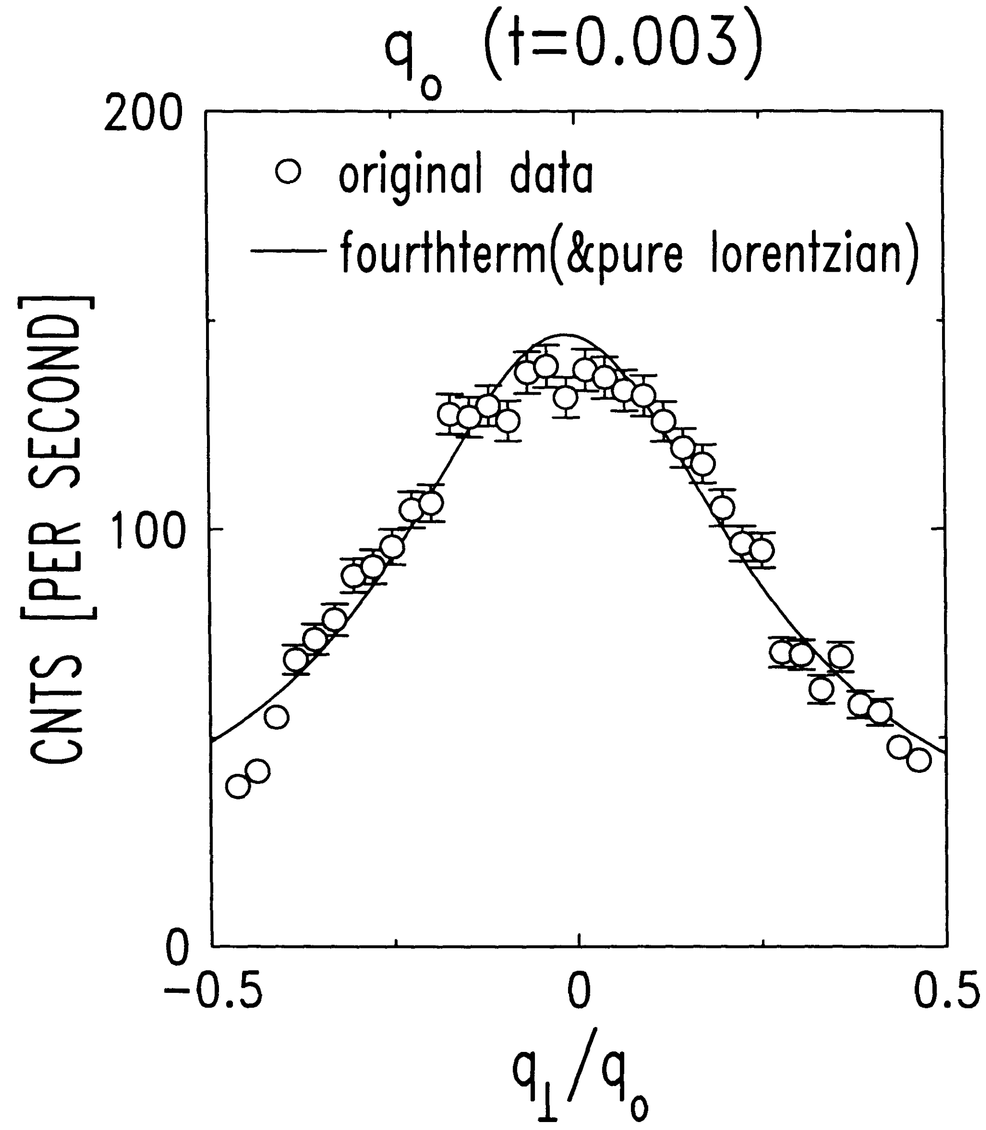

Figure 4-12: A typical transverse q_0 scan for the second sample. $t = 3\times10^{-3}$. Because the C_1 is fitted to be zero, the fourthterm fit and pure-lorentzian fit have no difference.

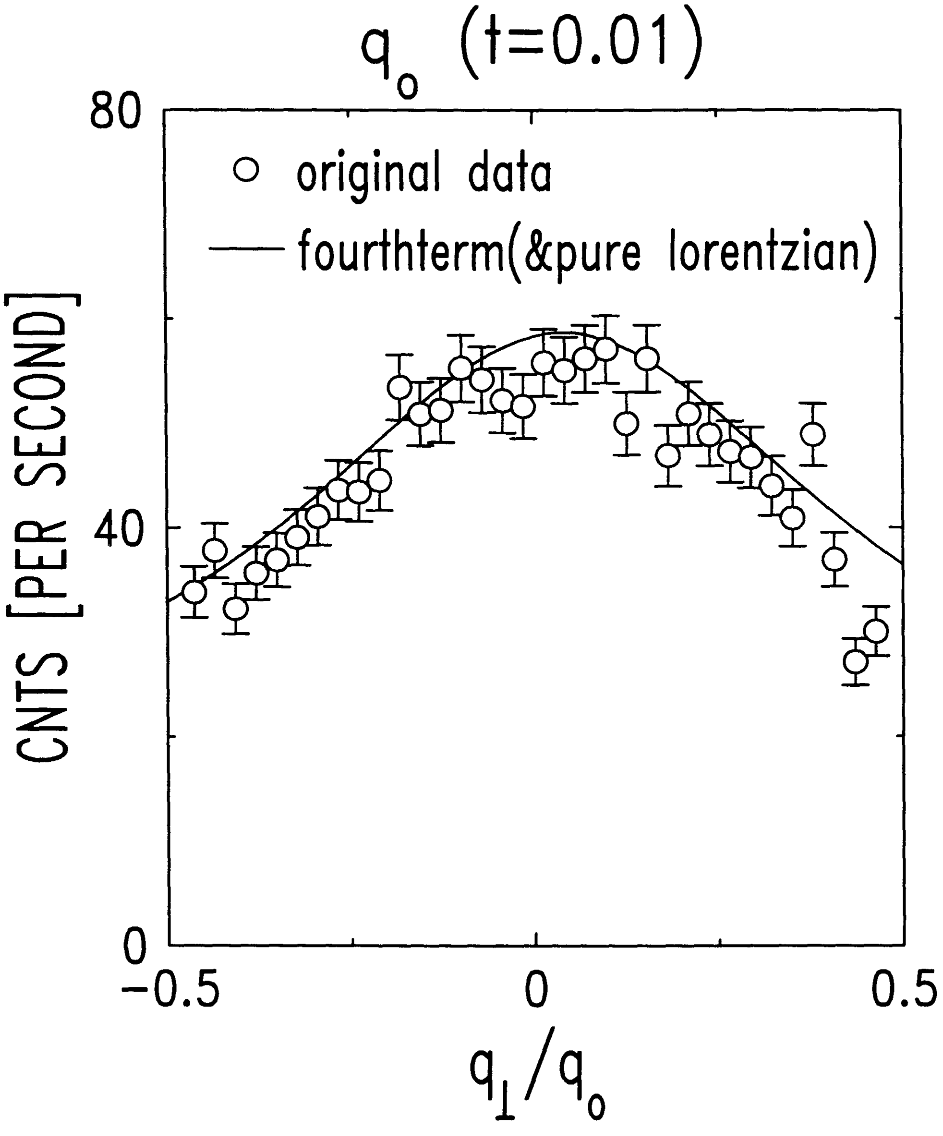

Figure 4-13: A typical transverse q_0 scan for the second sample. $t = 0.01$. Because the C_1 is fitted to be zero, the fourthterm fit and pure-lorentzian fit have no difference.

contradictory. As for the $2q_0$ profiles, they are well described by pure lorentzian for both samples (Fig. 4-14, Fig. 4-15, Fig. 4-16, Fig. 4-17, Fig. 4-18 and Fig. 4-19 for the first sample; Fig. 4-20, Fig. 4-21, Fig. 4-22, Fig. 4-23, Fig. 4-24 and Fig. 4-25 for the second sample). Simultaneous fits of the longitudinal and transverse scans yielded (χ_1,$\xi_{||1}$,$\xi_{\perp 1}$) and (χ_2,$\xi_{||2}$,$\xi_{\perp 2}$) for the peaks around q_0 and $2q_0$, respectively.

It is worthwhile to mention the theory developed by V.V.Lebedev. He described the $2q_0$ structure factor $S_2(\vec{q})$ with a new form. Namely,

$$S_2(\vec{q}) = S_{20}(\vec{q}) + \mu^2 S_{20}^2(\vec{q}) < \psi_1^2 \psi_1^{*2} >_{\vec{q}} \tag{4.2}$$

where the correlation function $< \psi_1^2 \psi_1^{*2} >_{\vec{q}}$ is associated with the first harmonic, and $S_{20}(\vec{q})$ is the bare value of the structure factor $S_2(\vec{q})$. $S_{20}(\vec{q})$ can be taken like

$$S_{20}(\vec{q}) = \frac{k_B T \chi_{20}}{1 + \xi_{||20}^2 (q_{||} - 2q_0)^2 + \xi_{\perp 20}^2 q_\perp^2} \tag{4.3}$$

where χ_{20}, $\xi_{||20}$ and $\xi_{\perp 20}$ are some coefficients which do not possess a critical behavior.

Basically, we accept Equ. 4.2 and Equ. 4.3. In fact, for $q_{||} = 2q_0$, $q_\perp = 0$, Equ. 4.2 becomes $S_2 = k_B T\chi_{20} + \mu^2 (k_B T \chi_{20})^2 \chi_2$, which is in a good agreement with our experiment. We also fitted our data with Equ. 4.2 (Fig. 4-14, Fig. 4-15, Fig. 4-16, Fig. 4-17, Fig. 4-18 and Fig. 4-19 for the first sample; Fig. 4-20, Fig. 4-21, Fig. 4-22, Fig. 4-23, Fig. 4-24 and Fig. 4-25 for the second sample). we can see that the Lebedev's second term has relatively small contribution, which further validate our pure lorentzian form for the $2q_0$ structure factor.

Susceptibility, correlation lengths and length anisotropies for the q_0 peak and the $2q_0$ peak in the nematic phase are shown in Fig. 4-26, Fig. 4-28, Fig. 4-27, Fig. 4-29, Fig. 4-30 and Fig. 4-31 together with the power law fits using $\chi(t) = \chi_0 t^{-\gamma}$, $\xi_{||}(t) = \xi_{||}^0 t^{-\nu_{||}}$, $\xi_\perp(t) = \xi_\perp^0 t^{-\nu_\perp}$ and $\xi_{||}/\xi_\perp \sim t^{-(\nu_{||}-\nu_\perp)}$, where $t = (T - T_c)/T_c$. Uncertainties in

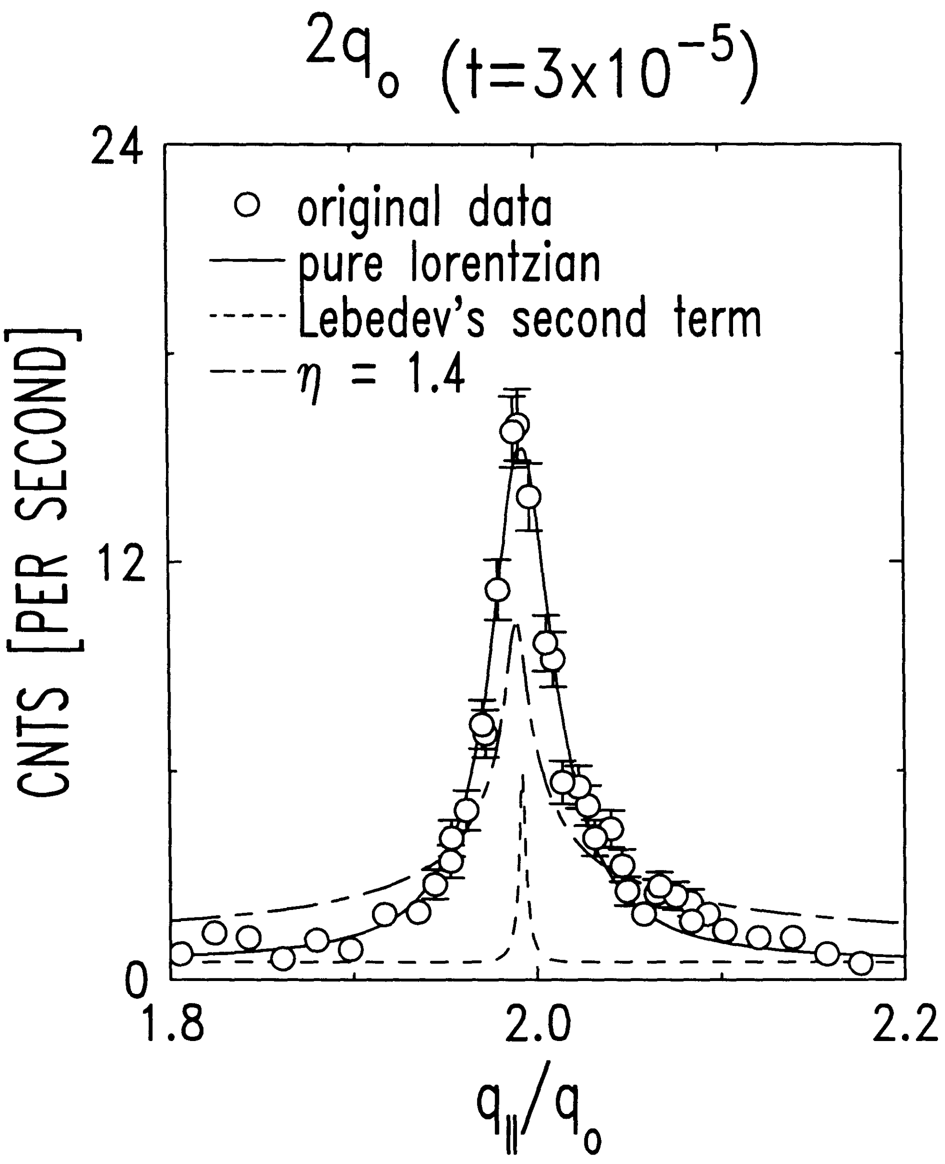

Figure 4-14: A typical longitudinal $2q_0$ scan for the first sample. $t = 3 \times 10^{-5}$. The — - line corresponds to the result of least-square fits by Equ. 4.7 with $\eta = 1.4$. The - - - line corresponds to the second term of Equ. 4.2.

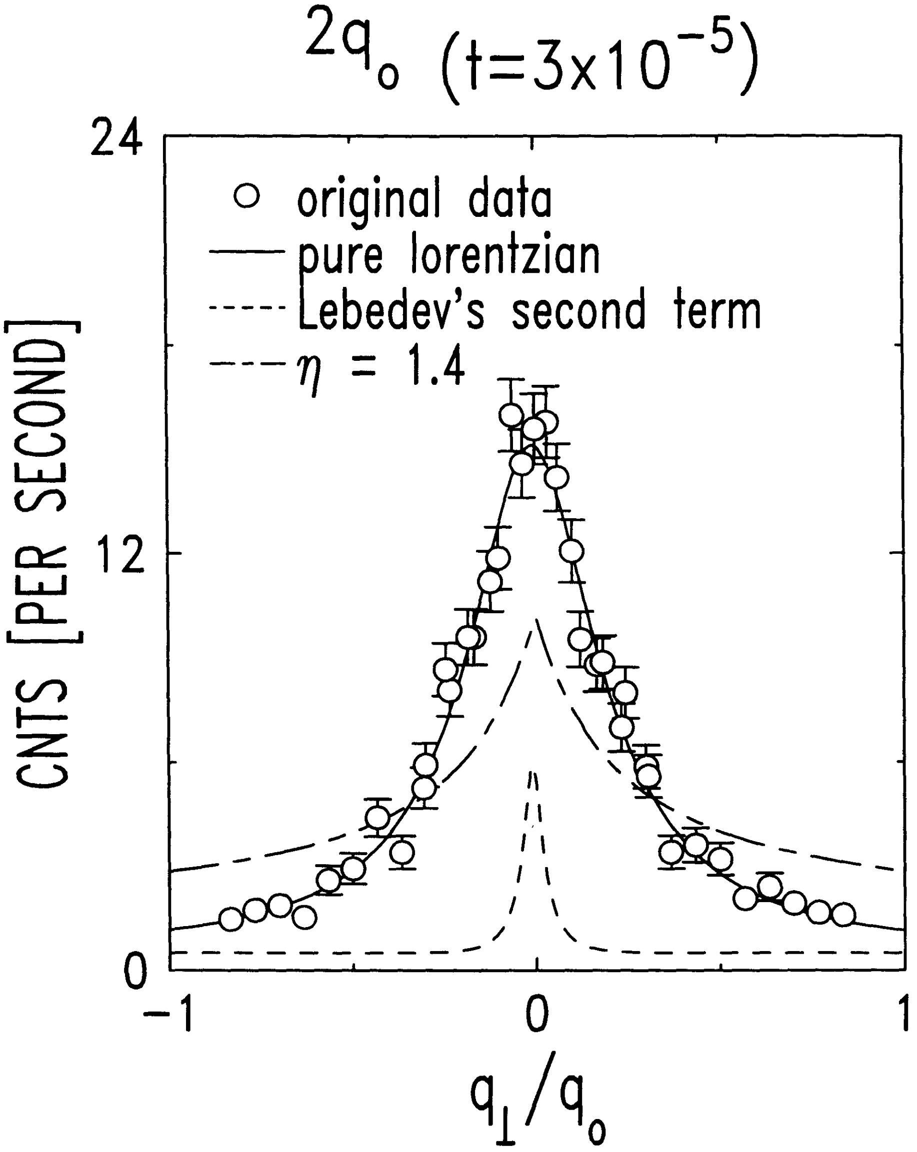

Figure 4-15: A typical transverse $2q_0$ scan for the first sample. $t = 3 \times 10^{-5}$. The — - line corresponds to the result of least-square fits by Equ. 4.7 with $\eta = 1.4$. The - - - line corresponds to the second term of Equ. 4.2.

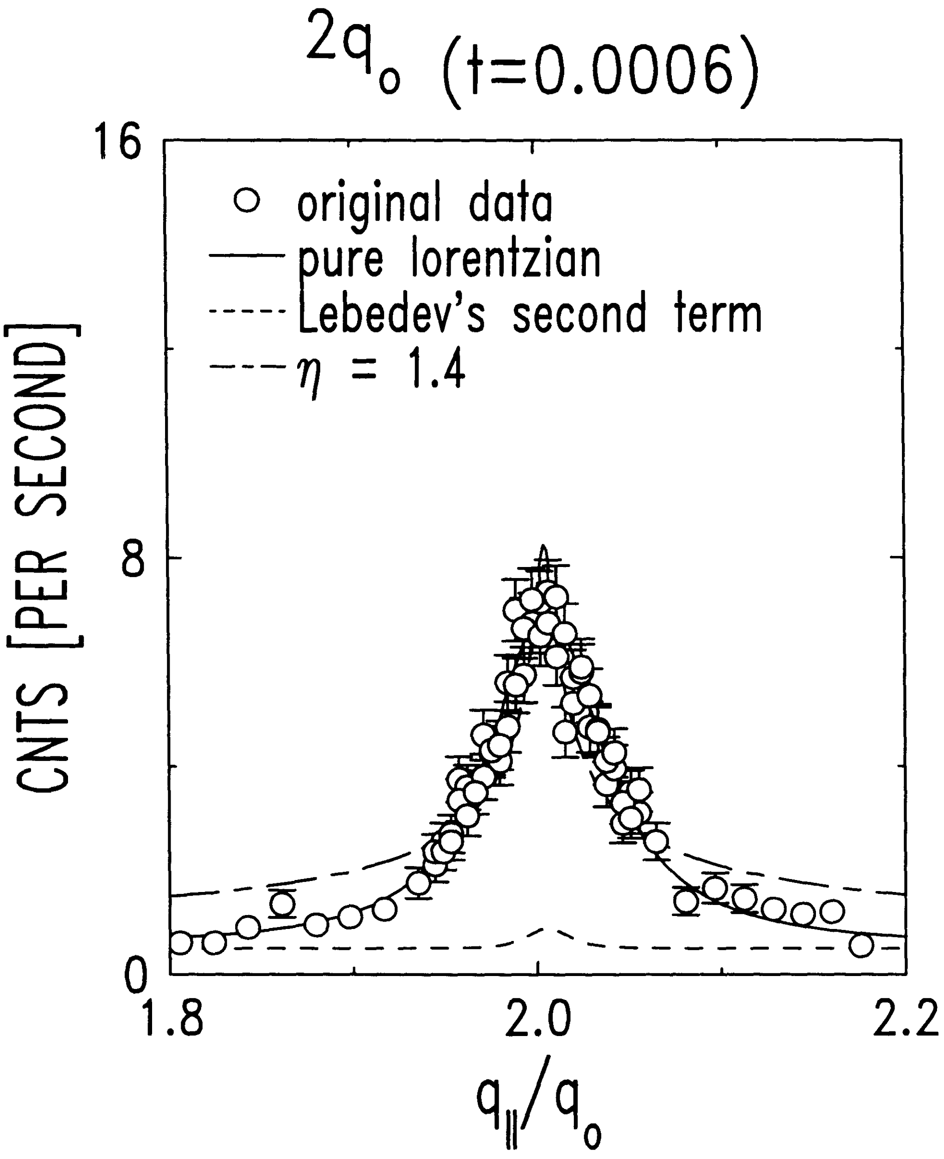

Figure 4-16: A typical longitudinal $2q_0$ scan for the first sample. $t = 6 \times 10^{-4}$. The — - line corresponds to the result of least-square fits by Equ. 4.7 with $\eta = 1.4$. The - - - line corresponds to the second term of Equ. 4.2.

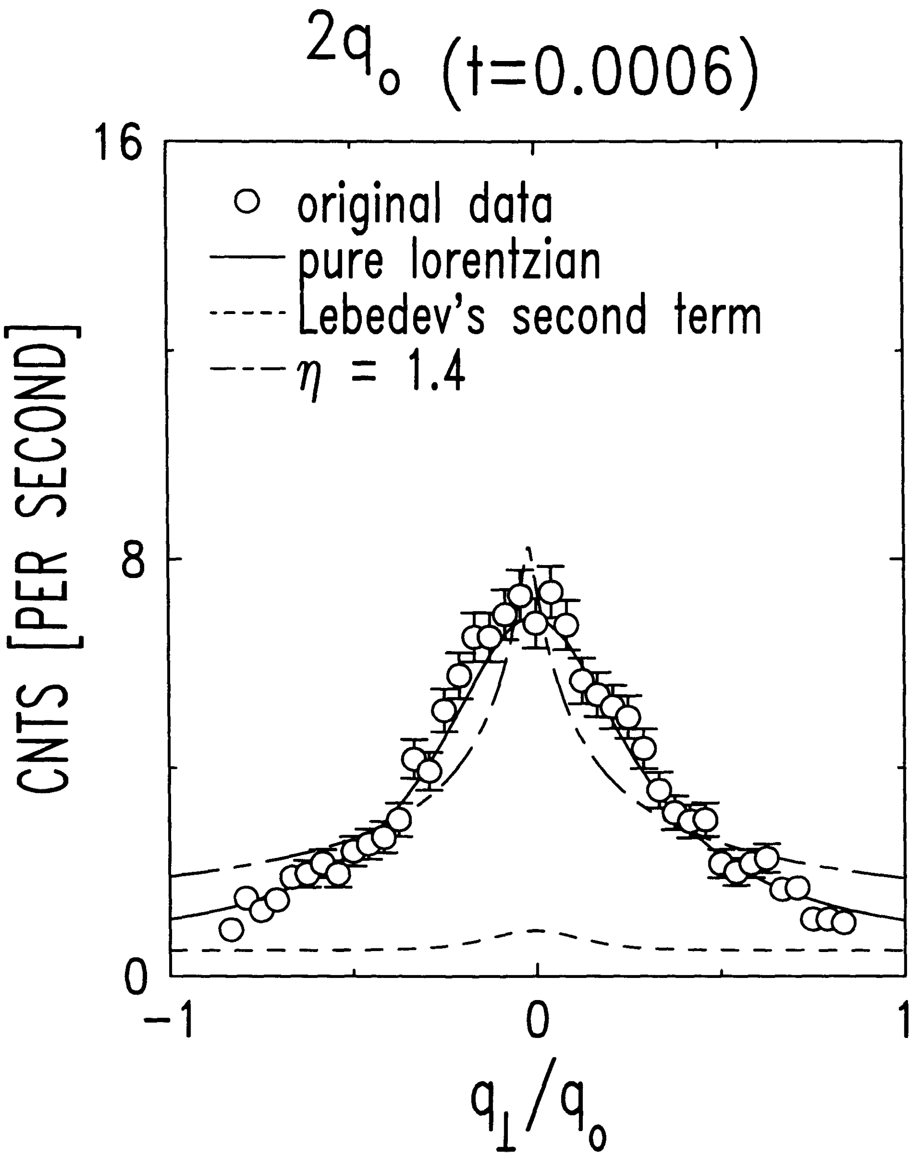

Figure 4-17: A typical transverse $2q_0$ scan for the first sample. $t = 6 \times 10^{-4}$. The — - line corresponds to the result of least-square fits by Equ. 4.7 with $\eta = 1.4$. The - - - line corresponds to the second term of Equ. 4.2.

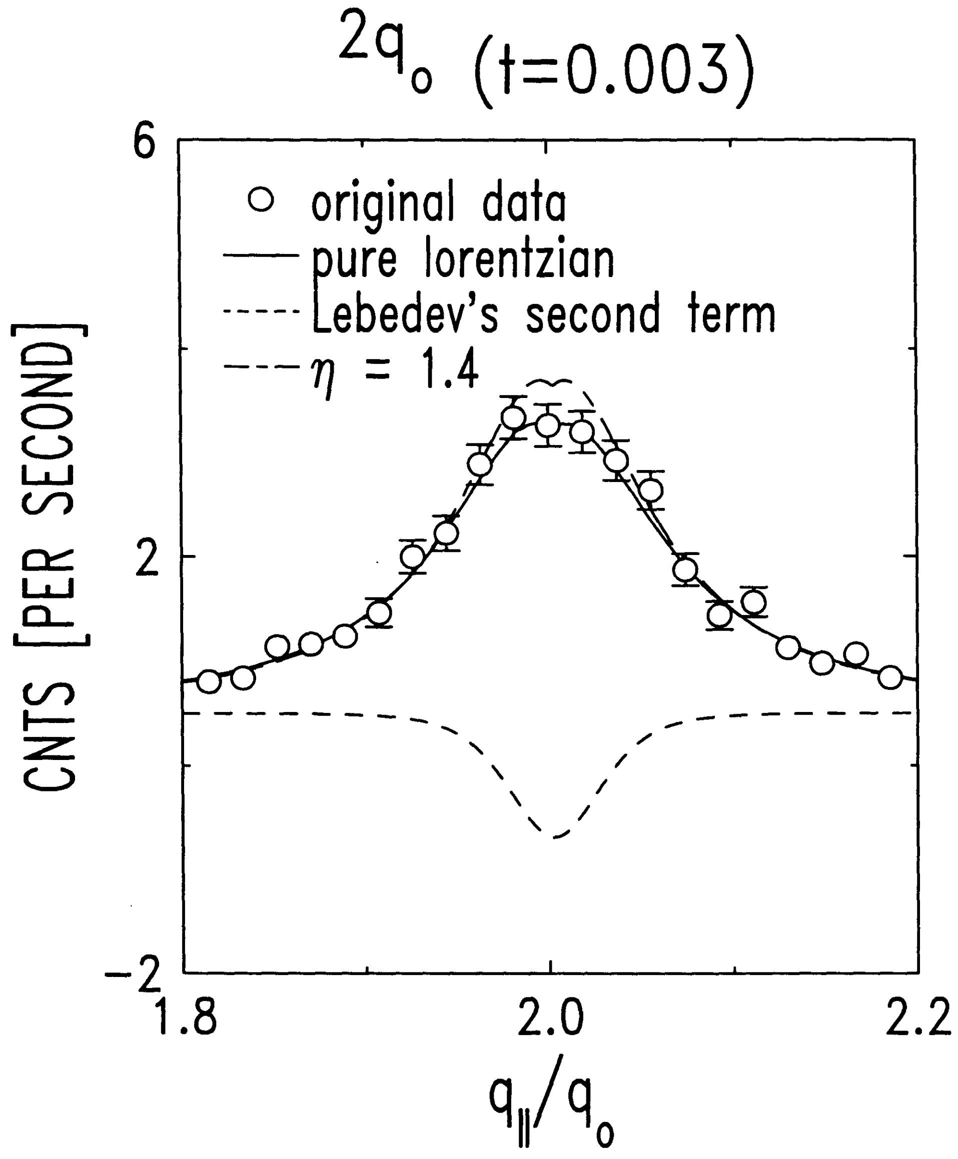

Figure 4-18: A typical longitudinal $2q_0$ scan for the first sample. $t = 3 \times 10^{-3}$. The — - line corresponds to the result of least-square fits by Equ. 4.7 with $\eta = 1.4$. The - - - line corresponds to the second term of Equ. 4.2.

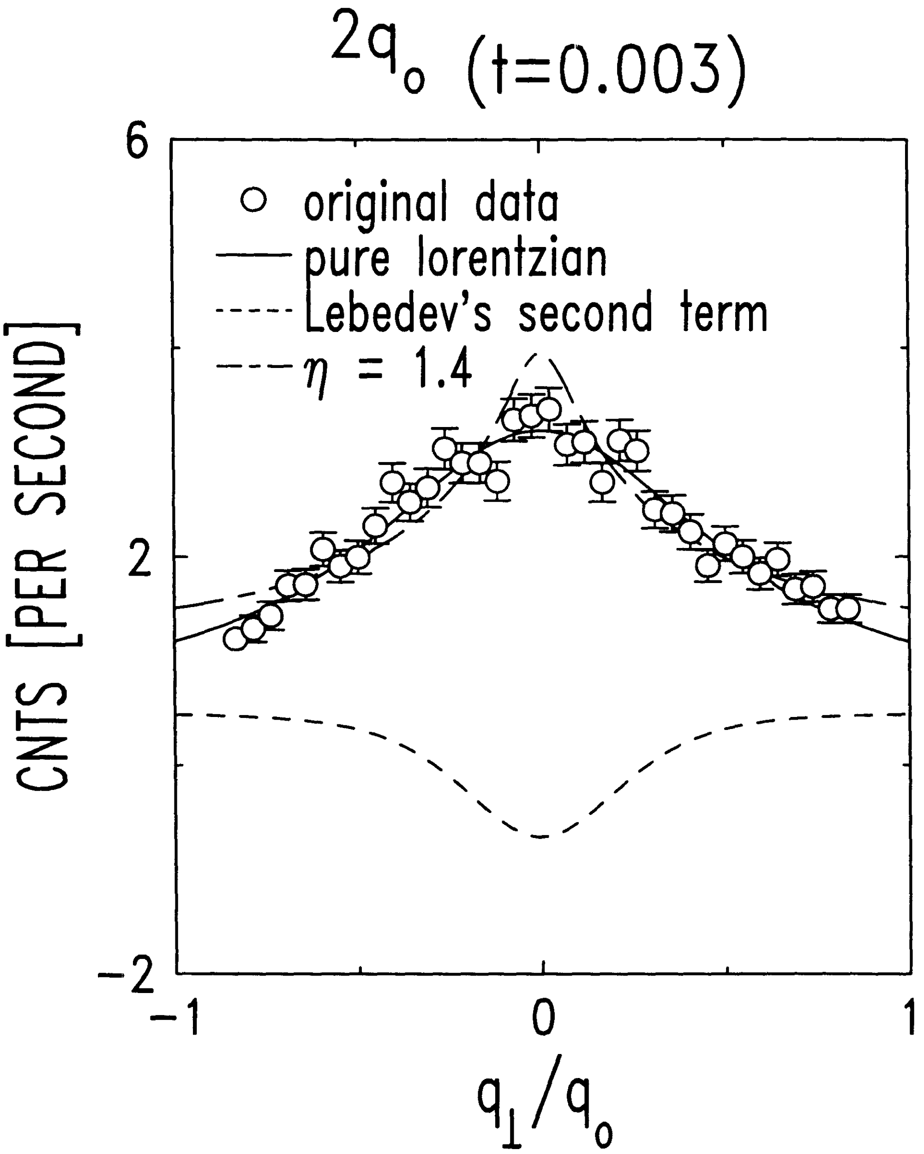

Figure 4-19: A typical transverse $2q_0$ scan for the first sample. $t = 3 \times 10^{-3}$. The — - line corresponds to the result of least-square fits by Equ. 4.7 with $\eta = 1.4$. The - - - line corresponds to the second term of Equ. 4.2.

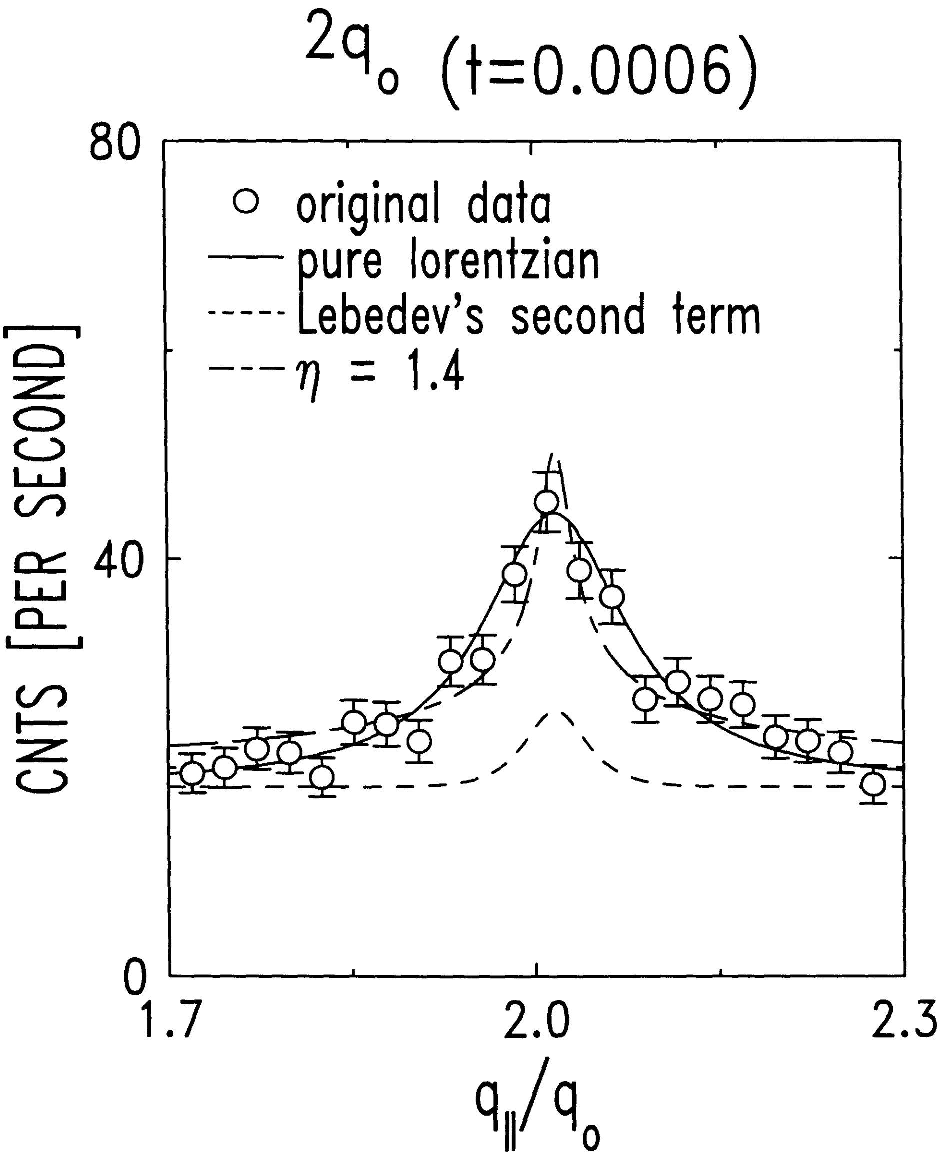

Figure 4-20: A typical longitudinal $2q_0$ scan for the second sample. $t = 6 \times 10^{-4}$. The — - line corresponds to the result of least-square fits by Equ. 4.7 with $\eta = 1.4$. The - - - line corresponds to the second term of Equ. 4.2.

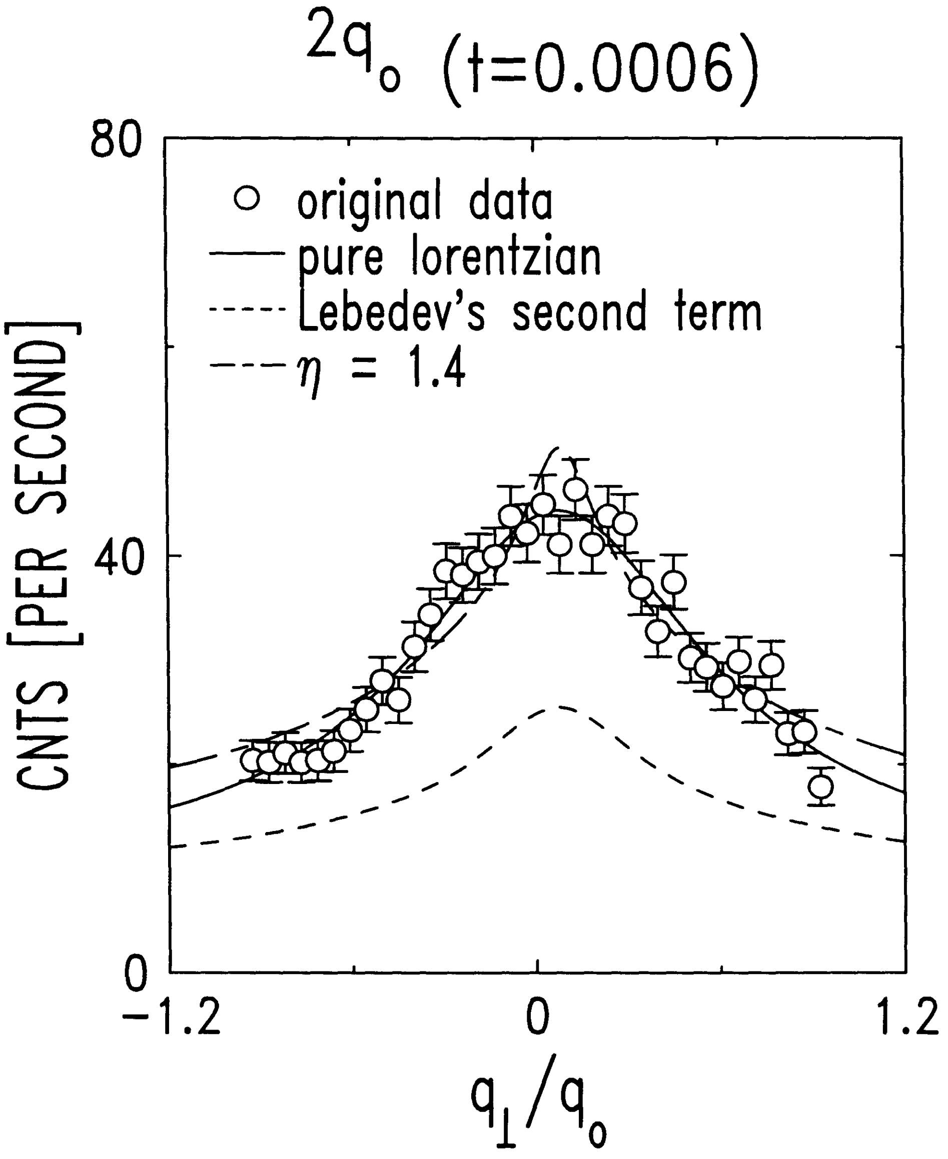

Figure 4-21: A typical transverse $2q_0$ scan for the second sample. $t = 6 \times 10^{-4}$. The — - line corresponds to the result of least-square fits by Equ. 4.7 with $\eta = 1.4$. The - - - line corresponds to the second term of Equ. 4.2.

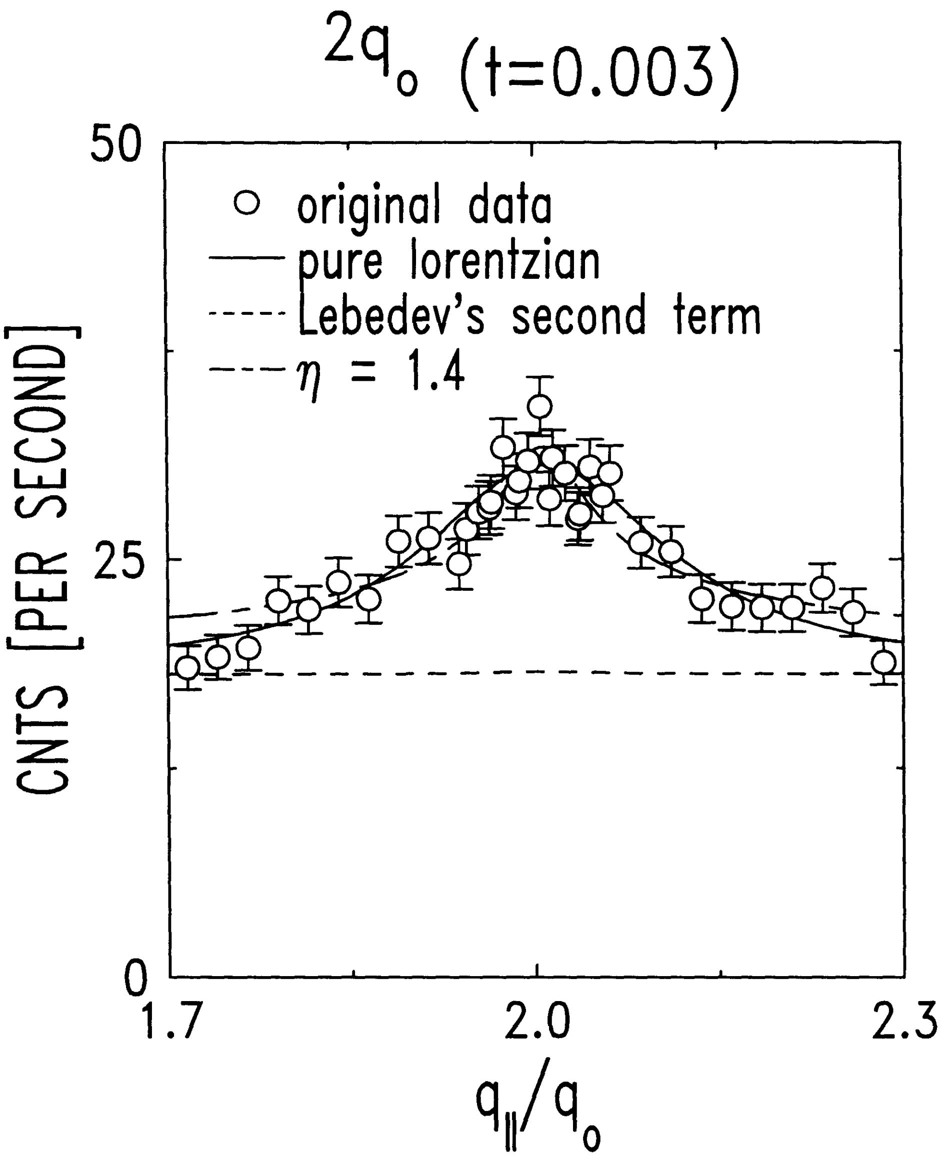

Figure 4-22: A typical longitudinal $2q_0$ scan for the second sample. $t = 3 \times 10^{-3}$. The — - line corresponds to the result of least-square fits by Equ. 4.7 with $\eta = 1.4$. The - - - line corresponds to the second term of Equ. 4.2.

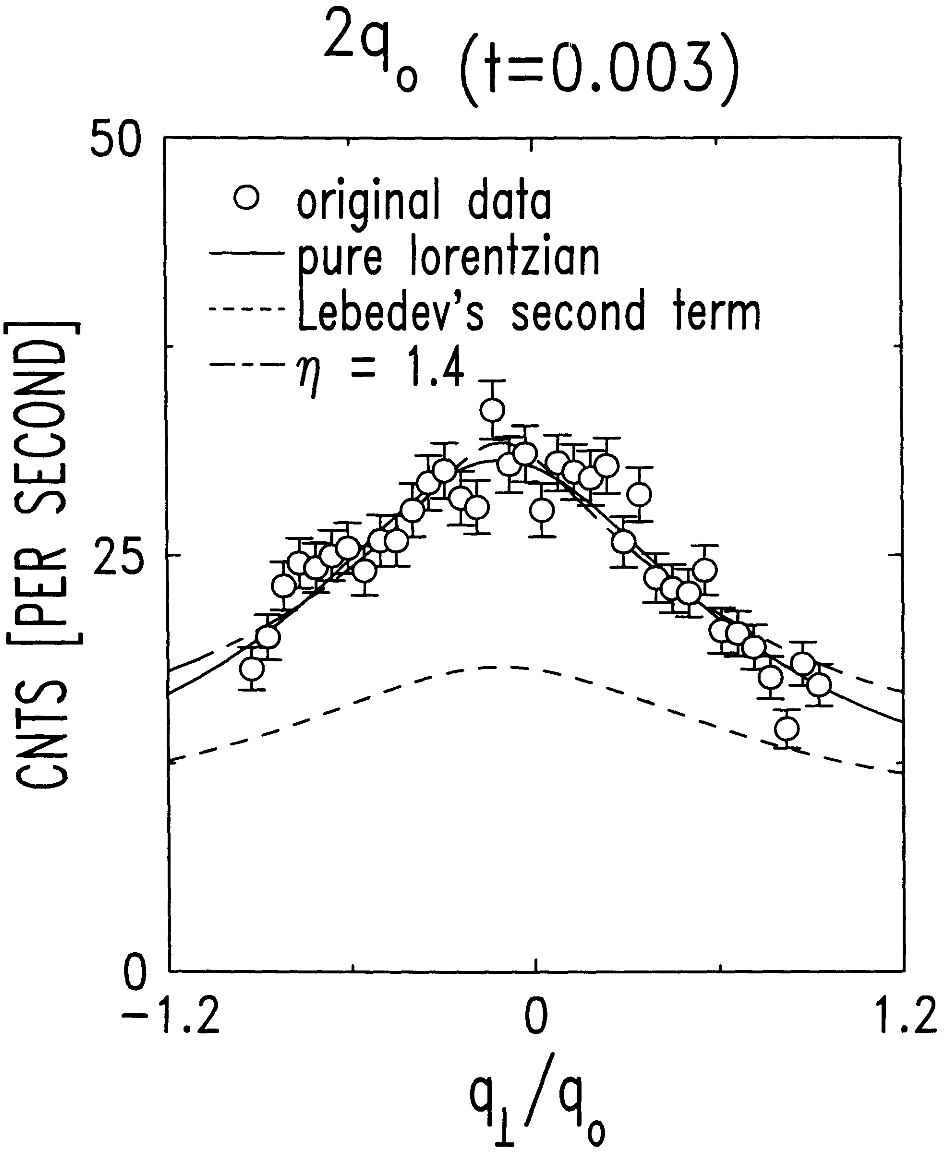

Figure 4-23: A typical transverse $2q_0$ scan for the second sample. $t = 3 \times 10^{-3}$. The — - line corresponds to the result of least-square fits by Equ. 4.7 with $\eta = 1.4$. The - - - line corresponds to the second term of Equ. 4.2.

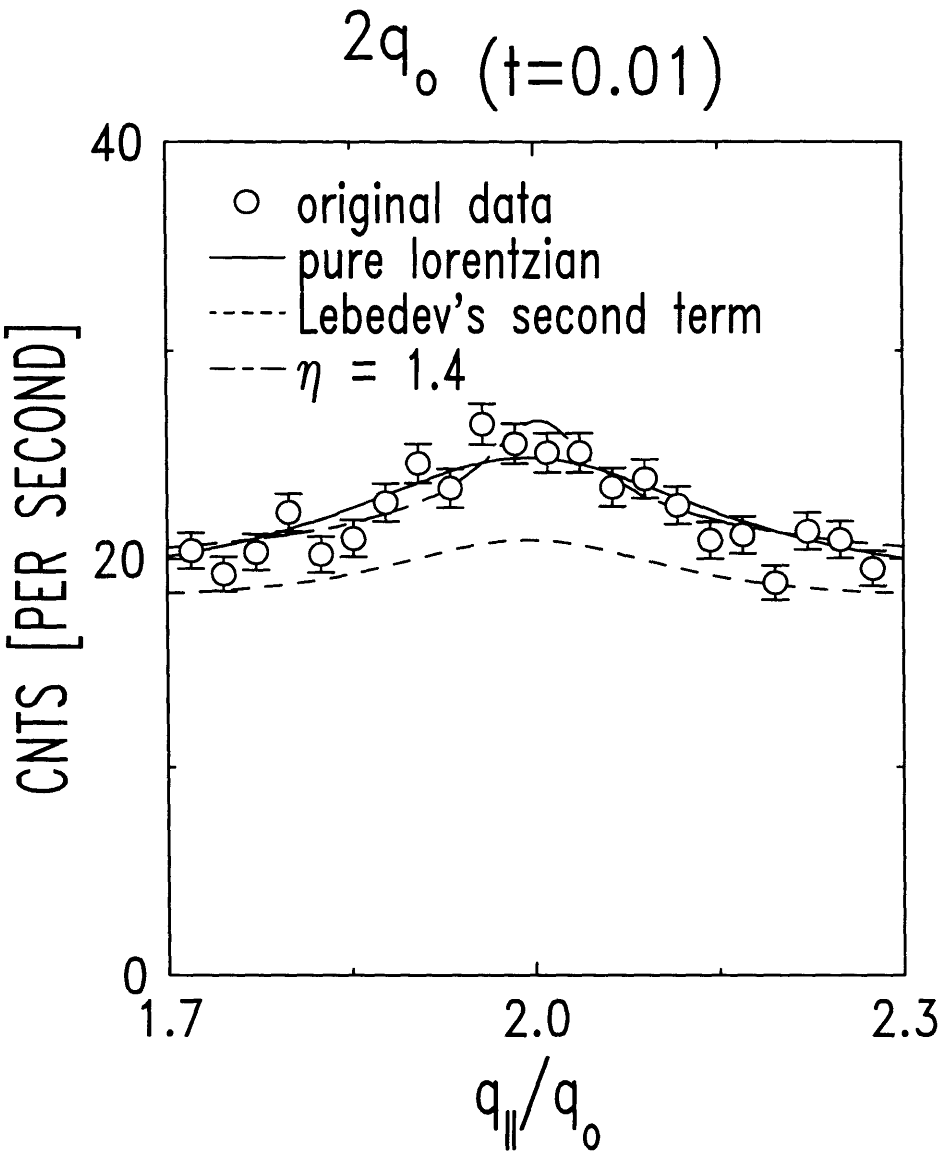

Figure 4-24: A typical longitudinal $2q_0$ scan for the second sample. $t = 0.01$. The — - line corresponds to the result of least-square fits by Equ. 4.7 with $\eta = 1.4$. The - - - line corresponds to the second term of Equ. 4.2.

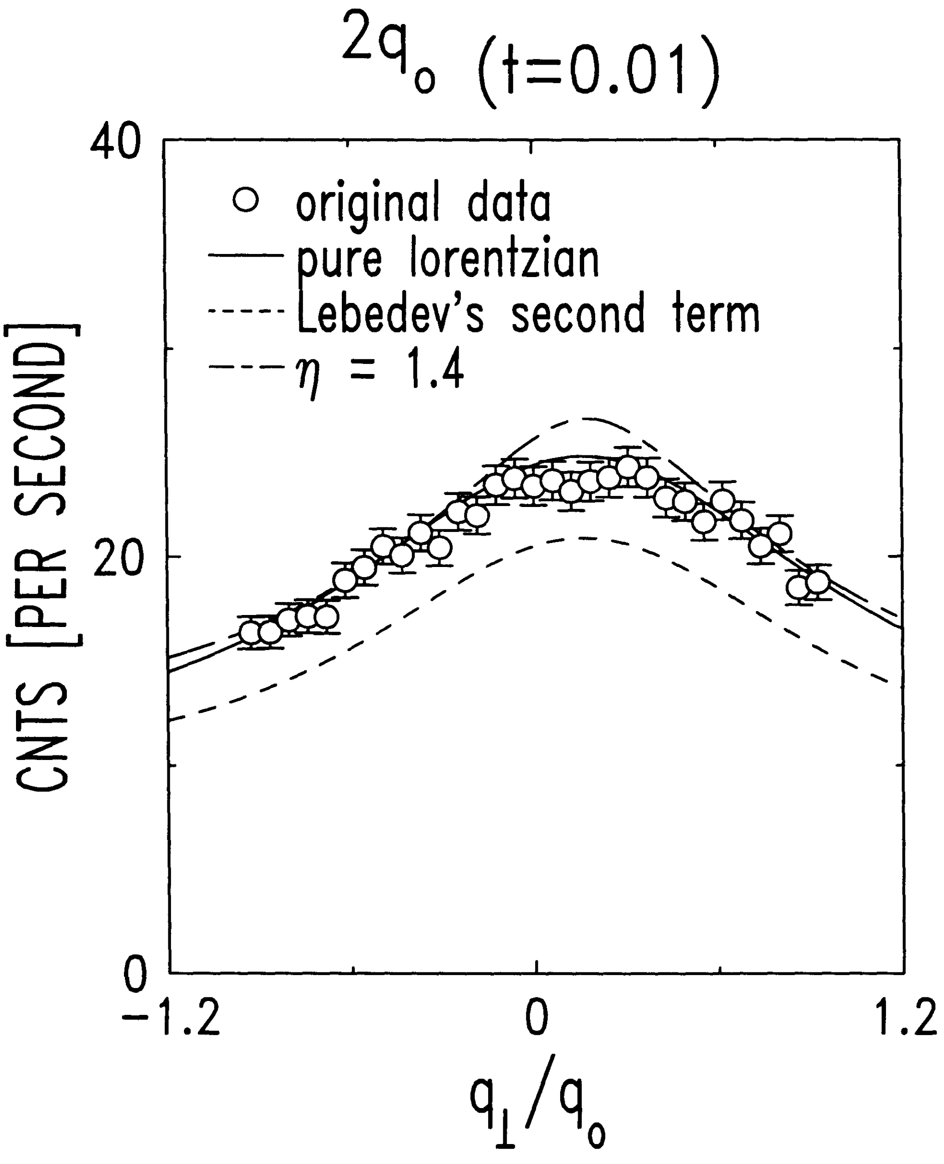

Figure 4-25: A typical transverse $2q_0$ scan for the second sample. $t = 0.01$. The — - line corresponds to the result of least-square fits by Equ. 4.7 with $\eta = 1.4$. The - - - line corresponds to the second term of Equ. 4.2.

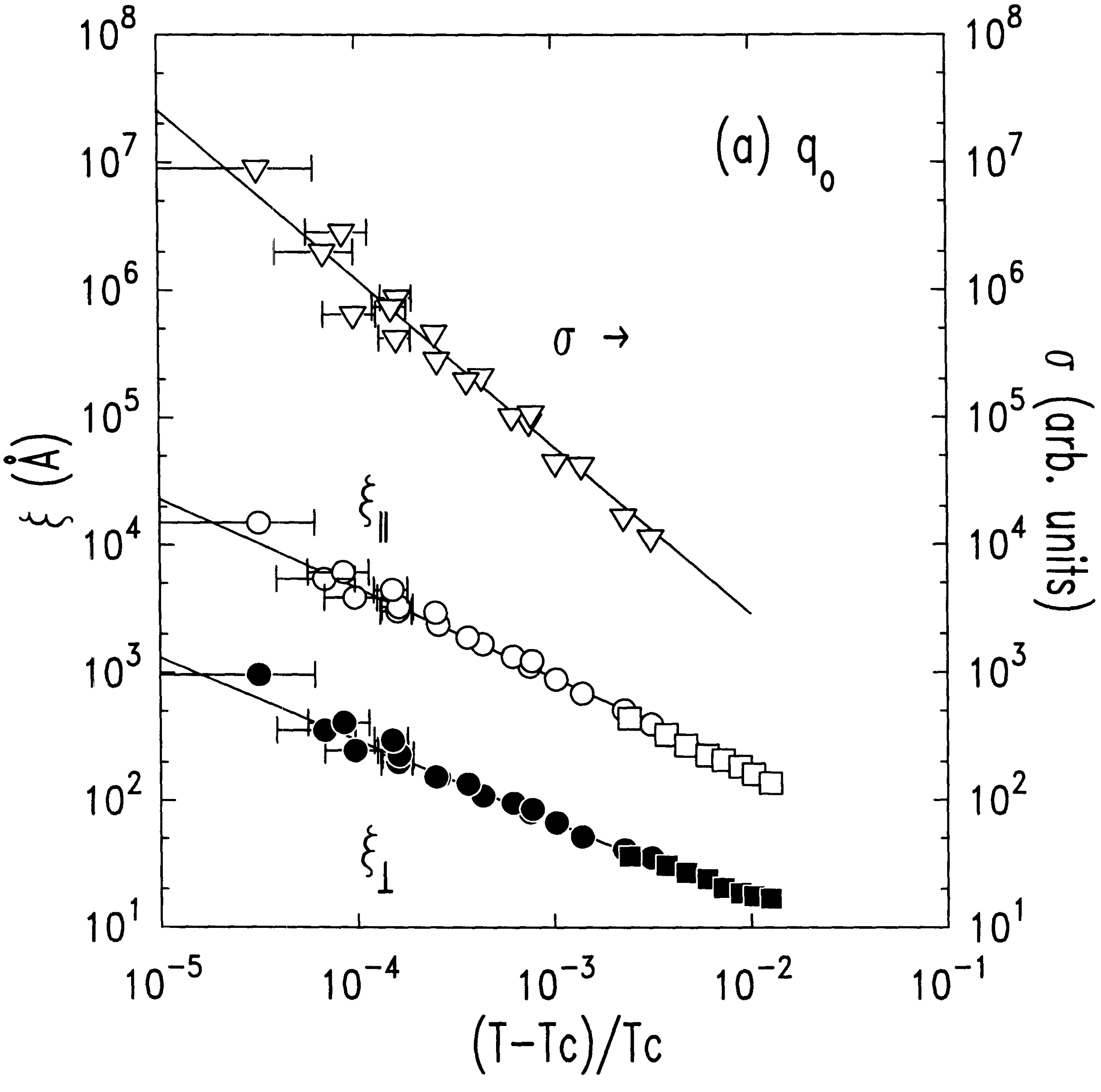

Figure 4-26: Susceptibility and correlation lengths for the q_0 peak in the nematic phase for the first sample.

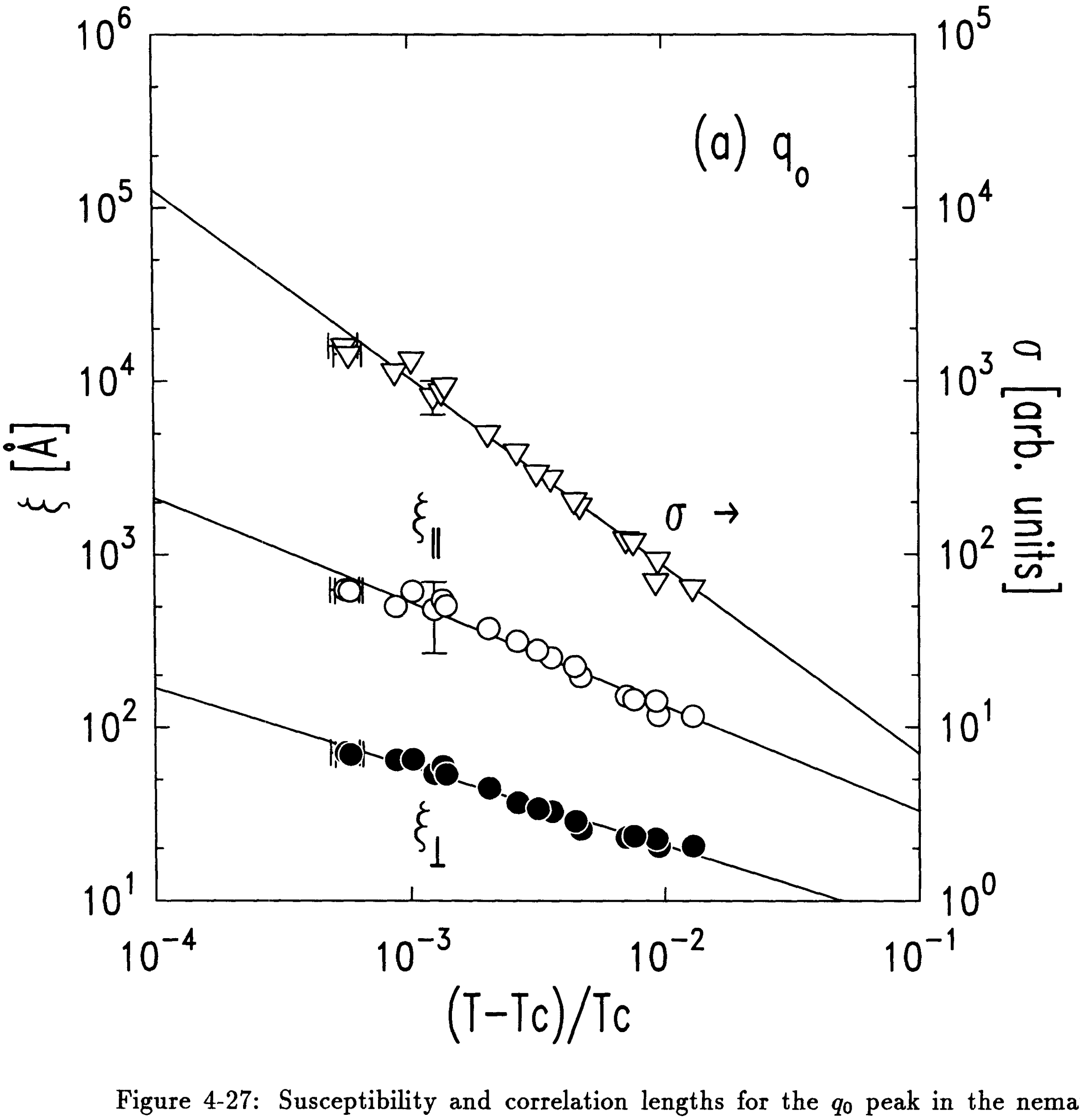

Figure 4-27: Susceptibility and correlation lengths for the q_0 peak in the nematic phase for the second sample.

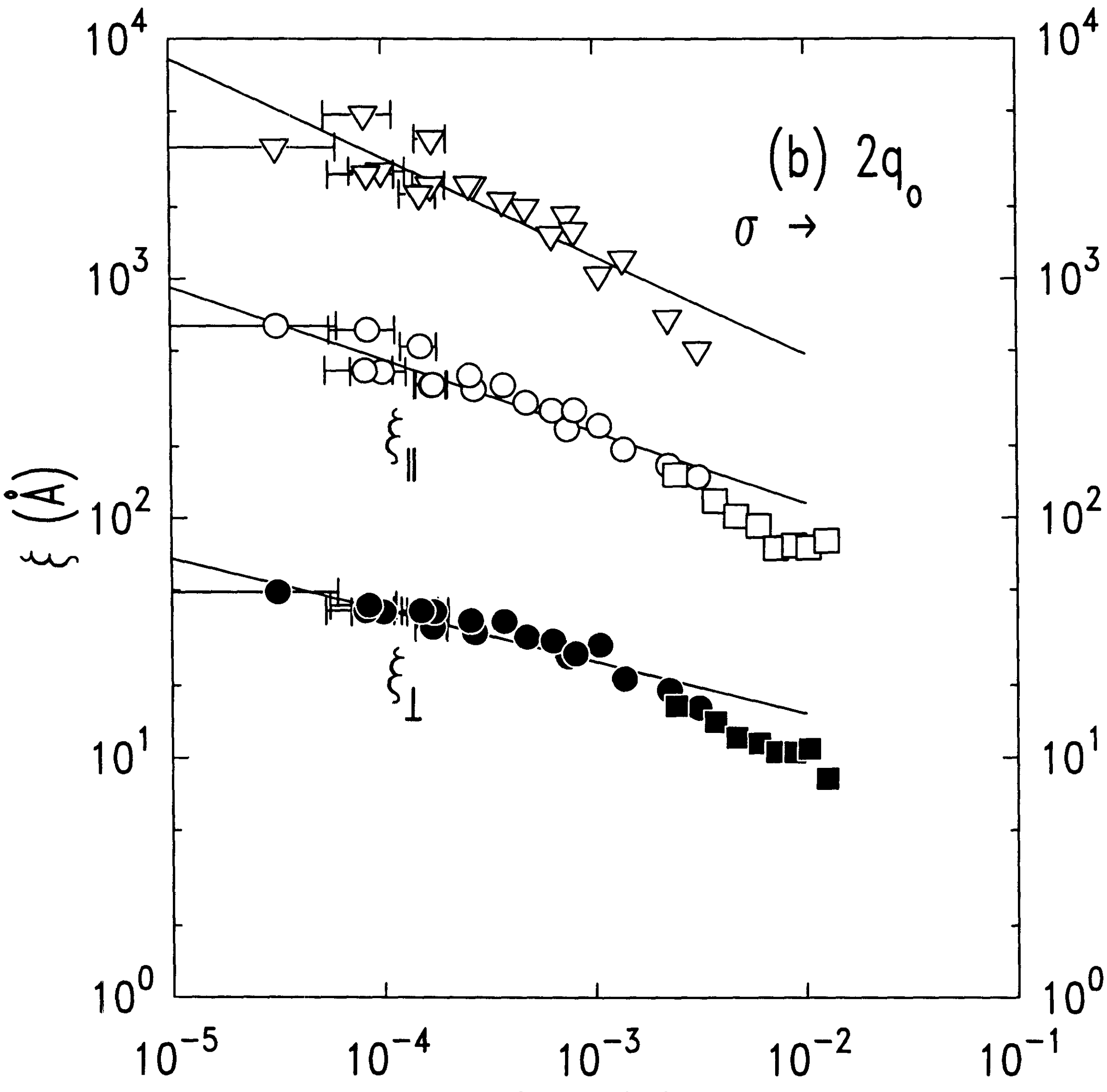

Figure 4-28: Susceptibility and correlation lengths for the $2q_0$ peak in the nematic phase for the first sample.

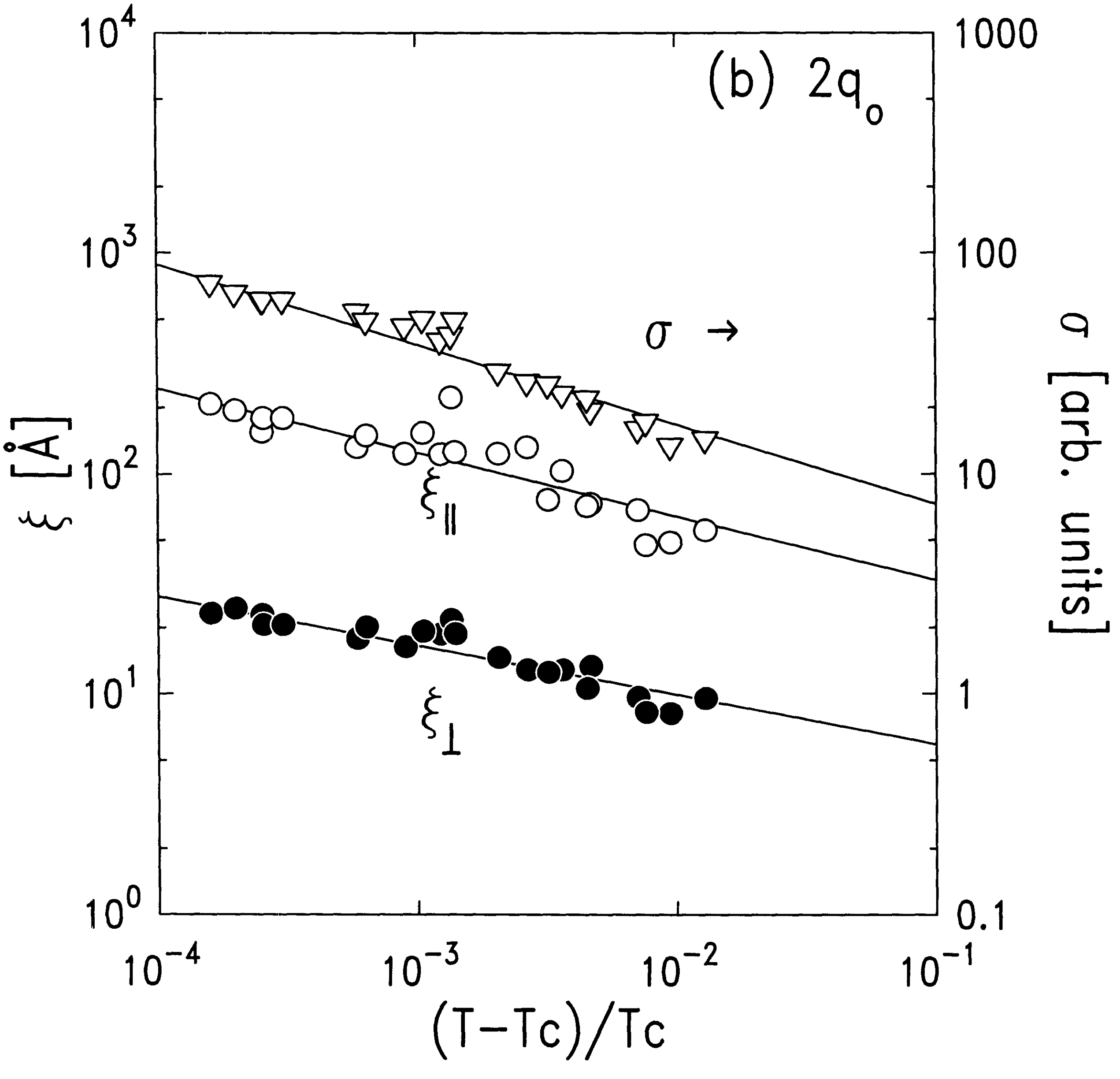

Figure 4-29: Susceptibility and correlation lengths for the $2q_0$ peak in the nematic phase for the second sample.

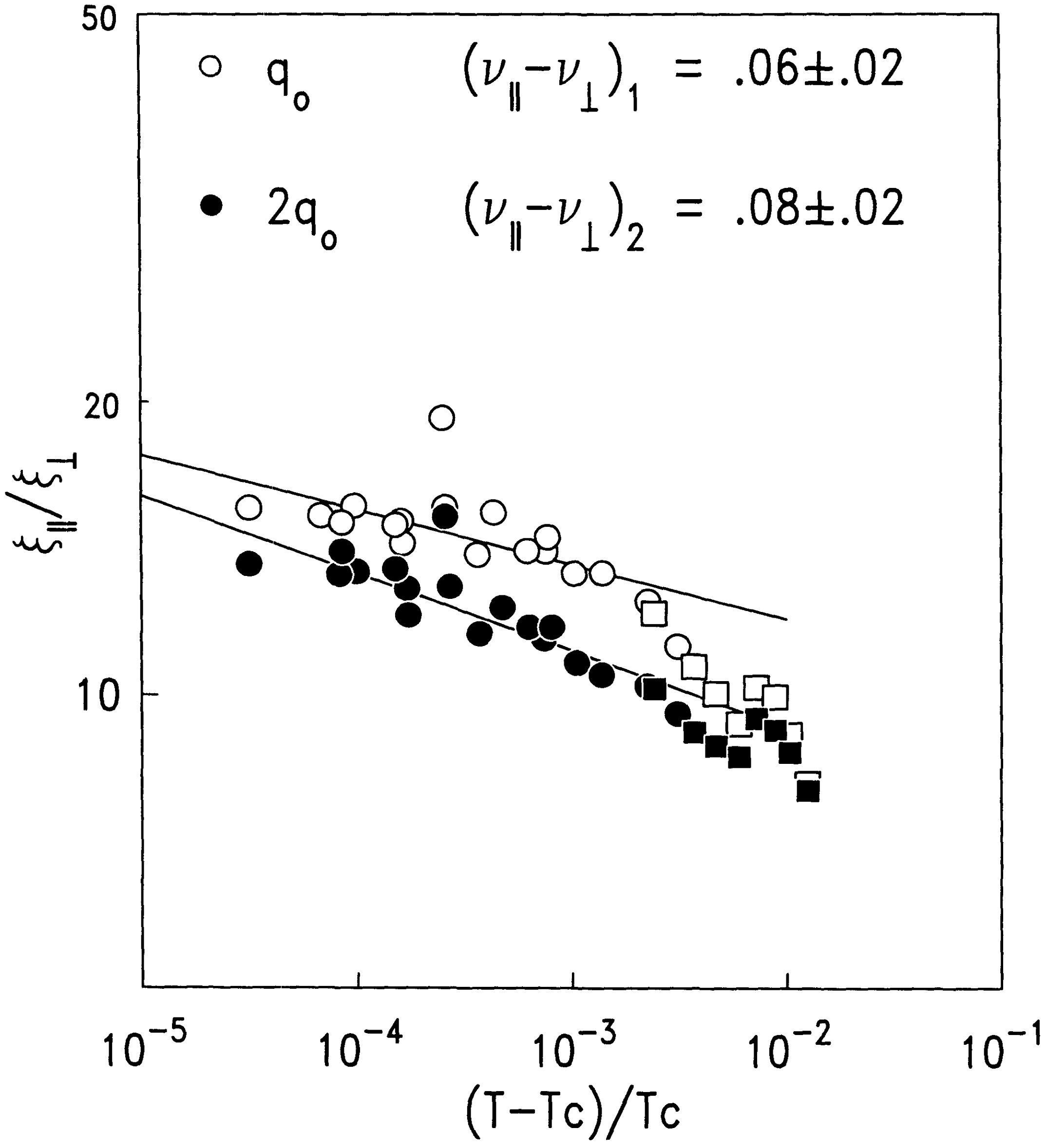

Figure 4-30: Length anisotropy: first sample

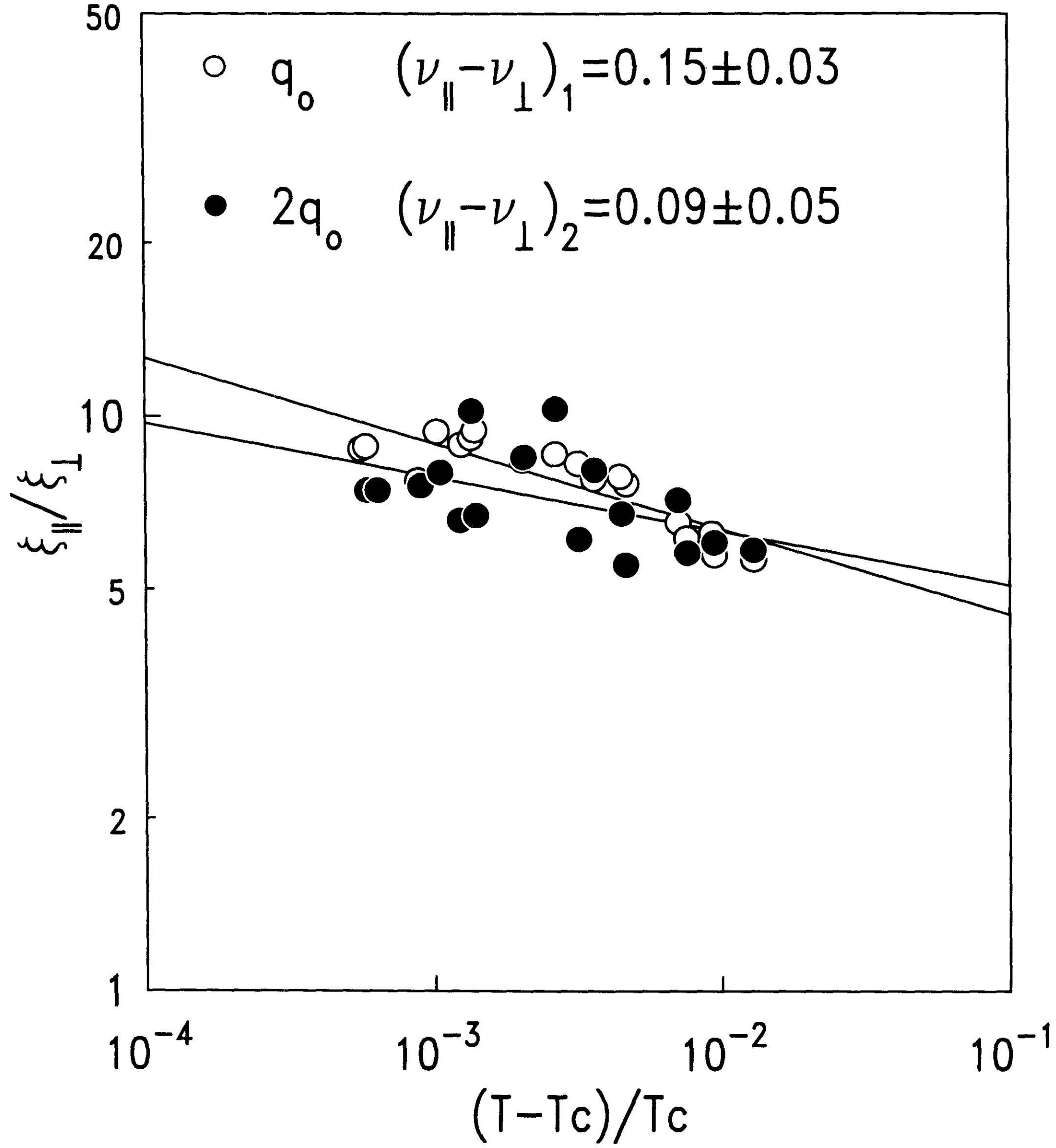

Figure 4-31: Length anisotropy: second sample

both t and χ or ξ are drawn. For most of the data, one standard deviation statistical errors in χ and ξ are smaller than the size of the plotted symbols. However, T-T$_c$ has a typical uncertainty of 0.012K for the first sample and an uncertainty of 0.031K for the second sample. These are due to the combined effects of the uncertainties in T$_c$ in a given run and the T$_c$ drift rate. For the first sample, we got the least squares values of the critical exponents as $\gamma_1 = 1.34 \pm 0.14$, $\nu_{\|1} = 0.70 \pm 0.07$, $\nu_{\perp 1} = 0.64 \pm 0.07$ and $(\nu_{\|1} - \nu_{\perp 1}) = 0.06 \pm 0.02$ for the q_0 peak and $\gamma_2 = 0.41 \pm 0.09$, $\nu_{\|2} = 0.31 \pm 0.04$, $\nu_{\perp 2} = 0.23 \pm 0.04$ and $(\nu_{\|2} - \nu_{\perp 2}) = 0.08 \pm 0.02$ for the $2q_0$ peak. Length anisotropies were obtained from fits to $\xi_{\|1}/\xi_{\perp 1}$ and $\xi_{\|2}/\xi_{\perp 2}$ directly. The q_0 exponent values agree within the errors with the 3D XY values $\gamma_{XY} = 1.316 \pm 0.002$ and $\nu_{XY} = 0.669 \pm 0.001$. In order to stress how closely these q_0 results are to 3D XY behavior, the lines shown in Fig. 4-26 represents fits with exponent value fixed at XY values $\gamma = \gamma_{XY}$, $\nu_{\|1} = \nu_{\perp 1} = \nu_{XY}$. We want to emphasize that we did not include the data represented by the square symbols in Fig. 4-26 and Fig. 4-28 when we did the fitting. These square-symbol data do not follow the general trend of the fitted lines. This is especially obvious in the $2q_0$ data. They fall far below the fitted lines (Fig. 4-28). We did not discuss these data in our previous paper [4]. The reason is that there were several days of synchrotron maintenance time between the circular-symbol data taking and square-symbol data taking. Basically, no experimentalist was around during that period. We suspect that something might then have happened during this interim period that changed the condition in the expriment. Is there really a crossover around $t \sim 10^{-3}$ or is it just a serendipitous phenomenon? Answering this question is exactly the motivation for us to do a similar albeit more controlled experiment on a second sample.

Fig. 4-27 and Fig. 4-29 shows no crossover in the entire t range covering the experiment. Quantitative data analysis yields $\gamma_1 = 1.09 \pm 0.24$, $\nu_{\|1} = 0.60 \pm 0.18$, $\nu_{\perp 1} = 0.46 \pm 0.12$, and $(\nu_{\|} - \nu_{\perp})_1 = 0.15 \pm 0.09$ for the q_0 peak and $\gamma_2 = 0.36 \pm 0.15$,

$\nu_{\|2} = 0.30 \pm 0.13$, $\nu_{\perp 2} = 0.22 \pm 0.10$ and $(\nu_{\|} - \nu_{\perp})_2 = 0.09 \pm 0.05$ for the $2q_0$ peak. The $2q_0$ exponent values agree quantitatively well with the values obtained for the first sample. However, the q_0 exponents are somewhat lower than 3d XY values. The major reason for these is that the T_c drifting rate was higher, resulting in a larger uncertainty in the reduced temperature. That explains why we have as a general feature for the q_0 scans of the second sample that the peak intensities for the $q_{\perp}$, $q_{\|}$ scans at the same temperature point are not the same(Fig. 4-5). Actual q_0 scans(for both $q_{\|}$ and $q_{\perp}$) took about 20 minutes. During this period, Tc was drifting with a high rate (30mk/hr), resulting in a change in the reduced temperature. Therefore, the peak intensities for $q_{\|}$ and $q_{\perp}$ are different.

As for $2q0$ scans of the second sample, we did not observe the peak intensity inconsistency(Fig. 4-6) because although the t was also changing during the $q_{\perp}$ and $q_{\|}$ scans, the $2q_0$ critical exponents have much smaller values than the respective ones for q_0(for example, $\gamma_2 \sim 0.4$, it is one third of γ_1, which is around 1.3.). Therefore, the effect of the change in T_c is much less important for the $2q_0$ data.

When we did the analysis for $2q_0$ scans at the second sample, we assume that the background to be a constant plus a lorentzian :

$$backgound = back + \frac{slope}{base^2 + (q_{\perp} - q_{\perp o})^2} \tag{4.4}$$

where we fixed back to be 8.9, slope to be 7.5, and base to be 0.9. These parameters were obtained by fitting them for several typical scans, then using the average values. The fits(Fig. 4-6) are excellent.

We conclude that within the Tc drift rate error, our experimental results for the second sample confirmed the results for the first sample. These are the best results one can get considering the large T_c uncertainty.

In addition to studying the diffuse scattering above T_c, we have measured the

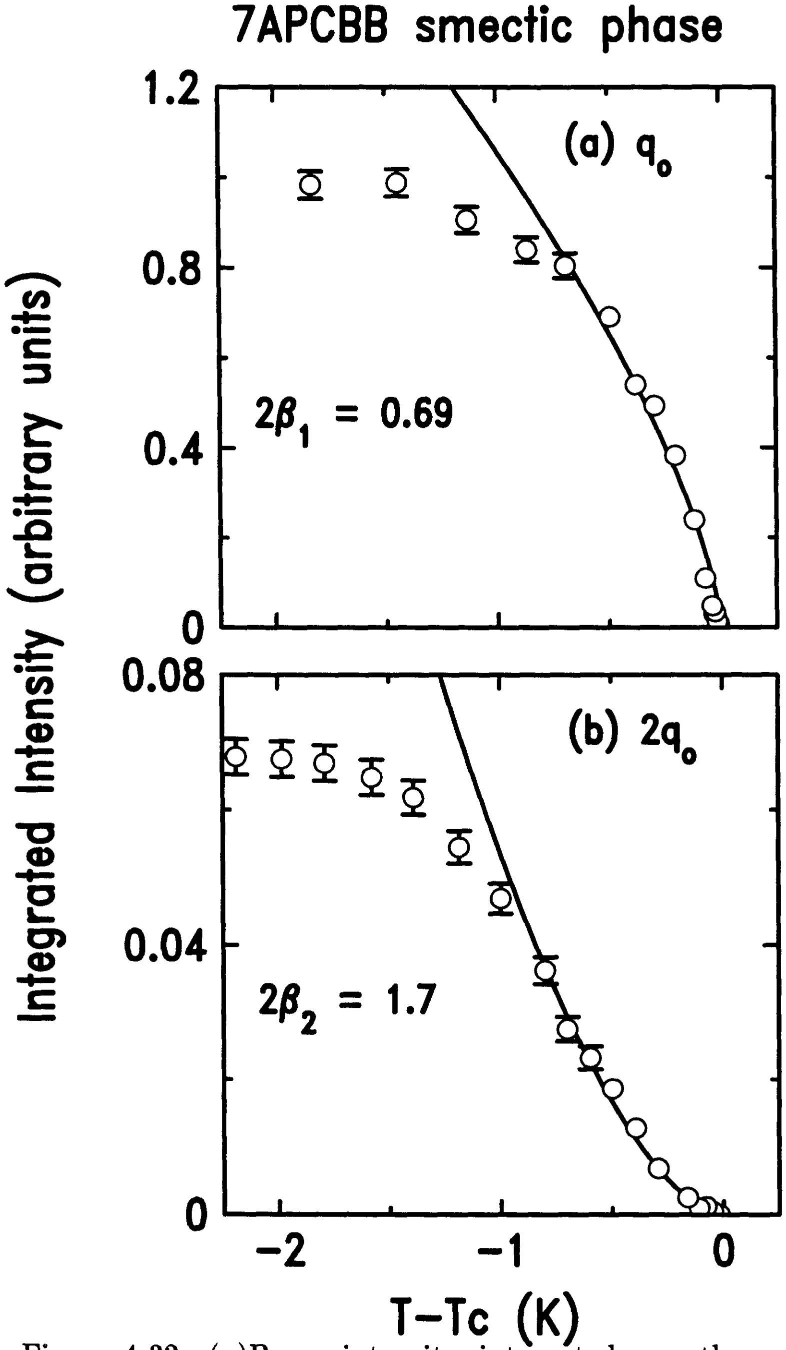

Figure 4-32: (a)Bragg intensity, integrated over the central mosaicity, versus temperature at q_0. The solid lline is a single power law $|T - T_c|^{2\beta_1}$ with $2\beta_1 = 0.69$; (b)Bragg intensity, integrated over the central mosaicity, versus temperature at $2q_0$. The Lorentz factor, $sin2\theta$, has been removed so that the relative intensity of (b) to (a) corresponds to $\sim |\Psi_2/\Psi_1|^2$ times the ratio of the molecular form factors squared. The solid line is a single power law $|T - T_c|^{2\beta_2}$ with $2\beta_2 = 1.7$.

integrated intensity $I(q_n) = \int d\vec{q}S(\vec{q} - n\vec{q}_0)$ of the quasi-Bragg peaks in the Sm-A$_2$ phase. The temperature dependences of $I(q_0)$ and $I(2q_0)$ are shown in Fig. 4-32, where the same arbitrary scale has been used for both intensities. Note that the ratio $I(2q_0)/I(q_0)(\sim |\Psi_2/\Psi_1|^2)$ in the Sm-A$_2$ phase is ~ 0.07 at $T = T_c - 2K$. This corresponds to a relative value for the order parameter of $|\Psi_2/\Psi_1| \sim 0.26$, the uncertainty arising from the molecular form factor which is not well known (for a discussion, see [6]). This may be compared with the value of $|\Psi_2/\Psi_1| \leq 0.001$ in the Sm-A phase of nonpolar 40.7 [6], which is typical of monolayer smectics.

The behavior of χ_2 in the nematic phase and $I(2q_0)$ in the $Sm - A_2$ phase can be quite well explained in terms of a scaling model for the behavior of harmonics of the free energy [7, 8, 9](see also the discussion in Chapter 1, Section 1.2): $F(t, h_n) \sim |t|^{2-\alpha} \sum_n g_n(h_n/|t|^{\phi_n})$ where ϕ_n is the crossover exponent for the nth harmonic. One immediately obtains

$$\Psi_n = \partial F/\partial h_n \sim |t|^{2-\alpha-\phi_n} \sim |t|^{\beta_n} \tag{4.5}$$

$$\chi_n = \partial^2 F/\partial h_n^2 \sim |t|^{2-\alpha-2\phi_n} \sim |t|^{-\gamma_n} \tag{4.6}$$

or $\beta_n = 2 - \alpha - \phi_n$ and $\gamma_n = -(2 - \alpha) + 2\phi_n$. The 3D XY value for ϕ_1 is 1.661, yielding $\beta_1 = 0.346$ and $\gamma_1 = 1.315$ as expected. The value of ϕ_2 is 1.16 ± 0.07 [7, 8, 9]. Thus $\beta_2 = 0.85 \pm 0.07$ and $\gamma_2 = 0.31 \pm 0.14$. This value of γ_2 is in good agreement with our experimental value $\gamma_2 = 0.41 \pm 0.09$ for the first sample or $\gamma_2 = 0.36 \pm 0.15$ for the second sample. As is evident in Fig. 4-32, the intensities for both q_0 and $2q_0$ begin to saturate at about 1K below T$_c$, presumably due to the pretranstional effects of the Sm-A$_2$-Sm-C$_2$ transition which occured at T$_c$-T $\sim 2.5K$ in this sample. Fits for the data to single power laws for $|T - T_c| < 0.8K$ yield $\beta_1 = 0.39 \pm 0.04$ and $\beta_2 = 0.76 \pm 0.04$ in reasonable agreement with the theoretical values $\beta_1 = 0.346 \pm 0.001$

and $\beta_2 = 0.85 \pm 0.07$. To emphasize this agreement, the lines in Fig. 4-32 are drawn with the 3D XY values for β_1 and β_2.

The behavior of $\xi_{\|2}$ and $\xi_{\perp 2}$ and the critical exponents $\nu_{\|2} \approx 0.3$, $\nu_{\perp 2} \approx 0.23$ is more difficult to explain. Following the theory in Chapter 1, Section 1.2, one expects that $\bar{\nu}_2 = \bar{\nu}_1 = \nu_{XY}$. If this were true, it would follow from $\gamma_n = (2 - \eta_n)\bar{\nu}_n$ that η_2 must be very different from $\eta_1 = \eta_{XY} \approx 0.03$. Using $\bar{\nu}_2 = \nu_{XY} = 0.669$ and $\gamma_2 = 0.31 \pm 0.14$ predicted from harmonic scaling theory, one obtains $\eta_2 = 1.5 \pm 0.2$, while the experimental $\gamma_2 = 0.41 \pm 0.09$(for the first sample) yields $\eta_2 = 1.4 \pm 0.2$ or $\gamma_2 = 0.36 \pm 0.15$(for the second sample) also yields $\eta_2 = 1.4 \pm 0.3$. In order to test this idea of large η_2 values, the $2q_0$ scattering peaks were re-analyzed with the form

$$S(2q_0) = \frac{k_B T \chi_2}{[1 + \xi_{\|2}^2 (q_\| - 2q_0)^2 + \xi_{\perp 2}^2 q_\perp^2]^{1-\eta_2/2}} \tag{4.7}$$

As illustrated in Fig. 4-14, Fig. 4-15, Fig. 4-16, Fig. 4-17, Fig. 4-18, Fig. 4-19 (for the first sample); Fig. 4-20, Fig. 4-21, Fig. 4-22, Fig. 4-23, Fig. 4-24 and Fig. 4-25 (for the second sample), when η_2 was fixed at 1.4 not even a qualitative fit to the scattering profiles was possible(especially at smaller t). Anisotropic hyperscaling, $\nu_{\|2} + 2\nu_{\perp 2} = 2 - \alpha$, is explicitly violated for the second-harmonic fluctuations.

Bibliography

[1] C. W. Garland, M. Meichle, B. M. Ocko, A. R. Kortan, C. R. Safinya, L. J. Yu, J. D. Litster, and R. J. Birgeneau, Phys. Rev. B **27**, 3234 (1983).

[2] J. Als-Nielsen, R. J. Birgeneau, M. Kaplan, J. D. Litster, and C. R. Safinya, Phys. Rev. Lett. **39**, 352 (1977).

[3] G. Nounesis, K. I. Blum, M. J. Young, C. W. Garland, and R. J. Birgeneau, Phys. Rev. E **47**, 1910 (1993).

[4] Lei Wu, M. J. Young, Y. Shao, C. W. Garland, and R. J. Birgeneau, Phys. Rev. Lett. **72**, 376 (1994).

[5] J. C. LeGuillon, and J. Zinn-Justin, Phys. Rev. B **21**, 3976 (1980).

[6] B. M. Ocko, A. R. Kortan, R. J. Birgeneau, and J. W. Goodby, J. Phys. (Paris) **45**, 113 (1984).

[7] A. Aharony, R. J. Birgeneau, J. D. Brock and J. D. Litster, Phys. Rev. Lett. **57**, 1012 (1986).

[8] R. A. Cowley, and A. D. Bruce, J. Phys. C **11**, 3577 (1978).

[9] J. D. Brock, D. Y. Noh, B. R. McClain, J. D. Litster, R. J. Birgeneau, A. Aharony, P. M. Horn, and J. C. Liang, Z. Phys. B **74**, 197 (1989).

Chapter 5

Conclusion

In summary, using synchrotron x-ray techniques it has been possible to measure the critical behavior above T_c associated with both the first and second-harmonic critical fluctuations. We have also measured the relative intensities of the first- and second-harmonic density wave order parameter scattering below T_c. We find that the first-harmonic critical behavior is 3D XY-like without any cross-over phenomenon, albeit with a small length anisotropy as is normally observed at N-Sm-A transitions. The second-harmonic susceptibility above T_c and the integrated Bragg intensity below T_c both are accurately predicted by the XY-model multicritical scaling theory [1, 2, 3]. However, the second-harmonic correlation lengths and exponents differ markedly from those characterizing the first harmonic. The scaling relation $\bar{\nu}_2(2-\eta_2) = \gamma_2$ is obeyed but anisotropic hyperscaling, $\nu_{\|2}+2\nu_{\perp 2} = 2-\alpha$, is severely violated. This result would appear to have important consequences for theories for all density wave systems. Is there a basic error in our current theoretical picture of density wave systems? Alternatively, is there a unique feature of the N-Sm-A_2 system which causes the violation of hyperscaling for the second-harmonic fluctuations [4]? Clearly, measurements of the higher-harmonic critical fluctuations in other density wave systems including most especially solid state materials such as $K_{0.3}MoO_3$, $NbSe_3$, and Cr are very important.

Further guidance from theory would also be helpful.

Bibliography

[1] A. Aharony, R. J. Birgeneau, J. D. Brock and J. D. Litster, Phys. Rev. Lett. **57**, 1012 (1986).

[2] R. A. Cowley, and A. D. Bruce, J. Phys. C **11**, 3577 (1978).

[3] J. D. Brock, D. Y. Noh, B. R. McClain, J. D. Litster, R. J. Birgeneau, A. Aharony, P. M. Horn, and J. C. Liang, Z. Phys. B **74**, 197 (1989).

[4] T. C. Lubensky, J. Chim. Phys. **80**, 31 (1983).